

Observational constraints and predictions of the interacting dark sector with field-fluid mapping

Joseph P Johnson, Archana Sangwan and S. Shankaranarayanan

Department of Physics, Indian Institute of Technology Bombay,
Mumbai 400076, India

E-mail: josephpj@iitb.ac.in, arch06san@gmail.com, shanki@phy.iitb.ac.in

Abstract. We consider an interacting field theory model that describes the dark energy - dark matter interaction. Only for a specific interaction term, this interacting field theory description has an equivalent interacting fluid description. For inverse power law potentials and linear interaction function, we show that the interacting dark sector model with field-fluid mapping is consistent with *four cosmological data sets* — Hubble parameter measurements (Hz), Baryonic Acoustic Oscillation data (BAO), Supernova Type Ia data (SN), and High redshift HII galaxy measurements (HIIG). More specifically, these data sets prefer a negative value of interaction strength in the dark sector and lead to consistent best-fit values of Hubble constant and other cosmological parameters. Having established that this interacting field theory model is consistent with cosmological observations, we obtain quantifying tools to distinguish between the interacting and non-interacting dark sector scenarios. We focus on the variation of the scalar metric perturbed quantities as a function of redshift related to structure formation, weak gravitational lensing, and the integrated Sachs-Wolfe effect. We show that the difference in the evolution becomes significant for $z < 20$, for all length scales, and the difference peaks at smaller redshift values $z < 5$. We then discuss the implications of our results for the upcoming missions.

Contents

1	Introduction	1
2	Interacting dark sector with field-fluid mapping: The model	3
3	Background evolution and observational constraints	4
3.1	Observational data	5
3.2	Data analysis technique	8
3.3	Parameter constraints	9
4	Evolution of the scalar perturbations and predictions of the model	16
4.1	Structure formation	18
4.2	Weak gravitational lensing	20
4.3	Integrated Sachs-Wolfe effect	23
5	Conclusions	24
6	Acknowledgements	26
A	Best fit values: ΛCDM, wCDM, and interacting dark sector models	26
B	Comparing the parameter constraints from JLA and Pantheon data sets	28
C	Parameter constraints for $U(\phi) \sim 1/\phi^2$	29
D	Evolution of scalar perturbations for ϕ^{-2} potential	29
D.1	Evolution of the scaled interaction function δq	29
D.2	Structure formation	29
D.3	Weak gravitational lensing	31
D.4	ISW effect	32
E	Sound speed of the scalar field	34

1 Introduction

Cosmological observations suggest that the energy budget of the Universe is dominated by dark energy and dark matter [1–6]. Λ CDM model provides the simplest description of the Universe dominated by dark energy and dark matter while being highly successful in describing various cosmological observations and phenomena like the cosmic microwave background (CMB) and nucleosynthesis [7–10]. But with the availability of high precision cosmological observational data, there have been some inconsistencies in the values of cosmological parameters estimated using the Λ CDM model, with the most prominent of them being the difference in the value of the Hubble’s constant estimated from the local distance measurements and CMB observations [6, 11–15]. These inconsistencies point towards the limitations of the Λ CDM model and the need for modifications to the standard model of cosmology.

Apart from the gravitational interaction, we know very little about the properties of dark matter and dark energy. Λ CDM model assumes that dark energy is constant in time. The quintessence model provides a more general time-varying dark energy represented by a scalar field [16, 17]. A quintessence dark energy model can be further generalized by introducing a non-gravitational interaction between dark energy and dark matter, which is not ruled out by cosmological observations [18–44]. Recently, it has been shown that the dark matter-dark energy interaction can reconcile the tensions in the estimated values of Hubble constant H_0 [45–51]. Hence it is important to develop the analytical and numerical tools to detect the interaction between dark energy and dark matter. For this purpose, we need a theoretical framework that provides a comprehensive description of the interacting dark sector.

In Ref.[52], two of the current authors, have explicitly constructed such a framework starting from a classical field theory action that describes interacting dark sector. The authors showed that: (i) A one-to-one mapping between the field theory description and the fluid description of the interacting dark sector exists for a unique interaction term. (ii) This class of interacting dark sector models has an attractor solution describing the accelerated expansion of the Universe. The establishment of such a mapping enables us to analyze the background and perturbed evolution of the Universe with dark energy - dark matter interaction.

To constrain the model parameters, especially the interaction strength, and to make testable predictions, one needs to specify the scalar field potential and the interaction function. In this work, we look at an inverse power law potential [53] $U(\phi) \sim 1/\phi^n$ where ($n = 1, 2$) and a linear interaction function $\alpha(\phi) \sim C\phi$ where $C \in [-1, 1]$. We constrain the cosmological and model parameters using Hubble parameter measurements (Hz) [54–61], high redshift HII Galaxy (HIIG) data [62–67], Baryon acoustic oscillation (BAO) data [68–72] and the Type Ia supernovae (SN) observations [73]. The key results are:

1. Although both negative and positive values of interaction strength (C) are allowed, observations show a preference for negative interaction strength ($C < 0$).
2. For our interacting dark sector model, the constraint on the Hubble constant from the combined data set is $H_0 = 69.79_{0.52}^{0.29}$ km s⁻¹Mpc⁻¹. This value lies between the value of Hubble constant reported by Planck is $H_0 = 67.5 \pm 0.5$ km s⁻¹Mpc⁻¹ which uses base Λ CDM cosmology [6] and the distance ladder estimates of Hubble constant is $H_0 = 73.48 \pm 1.66$ km s⁻¹ Mpc⁻¹ (from SH0ES data [14, 74]), and $H_0 = 74.03 \pm 1.42$ km s⁻¹Mpc⁻¹ (measurements of LMC Cepheids [15]). We also see that the constraint obtained from the individual data sets are consistent with each other.
3. The constraints on Ω_m obtained by the model are consistent with $\Omega_m = 0.31 \pm 0.007$ reported in [6] (for latest constraints on the cosmological parameters see [75–83] and the references therein).

Our analysis shows that, with respect to the low-redshift background observations, there is a strong degeneracy between the interacting and non-interacting dark sector models. To distinguish between the two scenarios, we need to go beyond the background evolution. In this work, we identify three specific tools that we can obtain by studying the difference in the evolution of cosmological perturbations in both of these scenarios [8, 10]: Structure formation, Weak gravitational lensing, and Integrated Sachs-Wolfe effect. More specifically, we look at the evolution of the density perturbation (δ_m), the Bardeen potential, and its derivative (Φ and Φ' respectively) for the inverse power law potential $U(\phi) \sim 1/\phi^n$ where ($n = 1, 2$) and

linear interaction function with negative interaction strength ($C < 0$). We evolve all the perturbed quantities in the redshift range $1500 \lesssim z < 0$. We see a significant difference in the evolution of the relevant perturbed quantities in the interacting and non-interacting scenarios, at all length scales, for $z < 20$. The maximum difference in the evolution is around $z \sim 5$. We thus explicitly show that it is possible to detect and constrain the interaction between dark energy and dark matter from cosmological observations.

In Sec. 2, we introduce the interacting dark sector model we have used for the analysis. In Sec. 3 we discuss the background evolution in the model and the numerical analysis using various observational data sets to obtain the parameter constraints. The evolution of the cosmological perturbations and their observational consequences are discussed in Sec. 4. In Sec. 5, we briefly discuss the results and discuss the implications of our analysis. Appendices A - E contain additional details.

In this work, we use the natural units where $m_{\text{pl}}^2 = G^{-1}$, and the metric signature $(-, +, +, +)$. Greek letters denote the four-dimensional space-time coordinates, and Latin letters denote the three-dimensional spatial coordinates. Unless otherwise specified, *dot* represents derivative with respect to cosmic time and *prime* denotes derivative with respect to number of e-foldings $N \equiv \ln a(t)$.

2 Interacting dark sector with field-fluid mapping: The model

In this work, we consider the model described by the action [52],

$$S = \int d^4x \sqrt{-g} \left(\frac{1}{16\pi G} R - \frac{1}{2} g^{\mu\nu} \nabla_\mu \phi \nabla_\nu \phi - U(\phi) - \frac{1}{2} e^{2\alpha(\phi)} g^{\mu\nu} \nabla_\mu \chi \nabla_\nu \chi - e^{4\alpha(\phi)} V(\chi) \right). \quad (2.1)$$

where ϕ corresponds to the dark energy and χ corresponds to the dark matter. The dark matter fluid in a homogeneous and isotropic Universe can be mapped to these scalar fields by defining the four velocity u_μ

$$u_\mu = - \left[-g^{\alpha\beta} \nabla_\alpha \chi \nabla_\beta \chi \right]^{-\frac{1}{2}} \nabla_\mu \chi, \quad (2.2)$$

the energy density (ρ_m) and pressure (p_m) of the dark matter fluid

$$p_m = -\frac{1}{2} e^{2\alpha} [g^{\mu\nu} \nabla_\mu \chi \nabla_\nu \chi + e^{2\alpha} V(\chi)], \quad \rho_m = -\frac{1}{2} e^{2\alpha} [g^{\mu\nu} \nabla_\mu \chi \nabla_\nu \chi - e^{2\alpha} V(\chi)]. \quad (2.3)$$

In this description, we can rewrite Einstein's equation in terms of dark energy scalar field and dark matter fluid:

$$G_{\mu\nu} = 16\pi G \left[\nabla_\mu \phi \nabla_\nu \phi - \frac{1}{2} g_{\mu\nu} \nabla^\sigma \phi \nabla_\sigma \phi - g_{\mu\nu} V(\phi) + p_m g_{\mu\nu} + (\rho_m + p_m) u_\mu u_\nu \right], \quad (2.4)$$

where the energy-momentum tensor for the dark matter fluid is given by

$$T_\nu^{(m)\mu} = p_m g_{\mu\nu} + (\rho_m + p_m) u_\mu u_\nu. \quad (2.5)$$

The interaction between the dark energy and the dark matter fluid is described by:

$$\nabla_\mu T_\nu^{(m)\mu} = Q_\nu^{(F)}, \quad (2.6)$$

where the interaction term is given by

$$Q_\nu^{(F)} = -e^{2\alpha(\phi)} \alpha_{,\phi}(\phi) \nabla_\nu \phi \left[\nabla^\sigma \chi \nabla_\sigma \chi + 4e^{2\alpha(\phi)} V(\chi) \right] = -\alpha_{,\phi}(\phi) \nabla_\nu \phi (\rho_m - 3p_m). \quad (2.7)$$

Identifying $T^{(m)} = T_\mu^{(m)\mu} = -(\rho_m - 3p_m)$, we get

$$Q_\nu^{(F)} = T^{(m)} \nabla_\nu \alpha(\phi). \quad (2.8)$$

The time component of $Q_\nu^{(F)}$ represents the energy transfer between dark energy and dark matter. It is important to know that the field-fluid mapping in Ref. [52] is valid only for the above form of $Q_\nu^{(F)}$. For easy reading, we denote $Q_0^{(F)}$ as Q . Q will be split into the background and perturbed parts given by $Q = \bar{Q} + \delta Q$.

To study the cosmological evolution and obtain predictions and constraints, we need to consider a specific form of scalar field potential $U(\phi)$ and the interaction function $\alpha(\phi)$. In this work, we focus on the quintessence dark energy model with an inverse power law potential [53] and a linear interaction function

$$U(\phi) \sim \frac{1}{\phi^n}, \quad \alpha(\phi) \sim \phi, \quad (2.9)$$

where $n = 1, 2$. The inverse power-law potential provides a self-consistent phenomenological description of DE whose density decreases as the Universe expands, but decreases less rapidly than the nonrelativistic (cold dark, and baryonic) matter density in a spatially flat universe [53]. The above interaction function is the simplest form for obtaining the interacting dark sector considered in this work from a field theory action.

3 Background evolution and observational constraints

We consider a spatially flat universe governed by Friedmann equations

$$\left(\frac{\dot{a}}{a}\right)^2 = \frac{8\pi G}{3} \rho_{tot}, \quad \ddot{a} = -\frac{4\pi G}{3} (\rho_{tot} + 3P_{tot})$$

where ρ_{tot} and P_{tot} denote the total energy density and pressure of the universe at a given time. At late times, the contribution of the relativistic matter density (ρ_r) is negligible as compared to the dark (non-relativistic) matter (ρ_m) and dark energy density (ρ_ϕ). Hence, for the analysis in this section, we neglect ρ_r and total density is $\rho_{tot} = \rho_m + \rho_\phi$.

The dynamics of the scalar field is governed by

$$(\ddot{\phi} + 3H\dot{\phi} + U_{,\phi})\dot{\phi} = \bar{Q},$$

where, \bar{Q} is the background interaction term. Here, ϕ is in the units of $m_{\text{Pl}} = G^{-1/2}$. The scalar field potential is assumed to be

$$U(\tilde{\phi}) = \frac{\kappa}{2} m_{\text{Pl}}^2 \tilde{\phi}^{-n} \quad (3.1)$$

where κ is of the order of unity. To make the analysis simpler, we rescale the scalar field ϕ to $\tilde{\phi} = \sqrt{16\pi G} \phi$. Note that $\tilde{\phi}$ is dimensionless.

The evolution of non-relativistic matter density is given by

$$\dot{\rho}_m + 3H\rho_m = -\bar{Q},$$

where we have considered a pressureless dark matter fluid, $p_m = 0$. For the interaction term, $\bar{Q} = -\alpha_{,\phi}\dot{\phi}\rho_m$, the above equation gives, $\rho_m = \rho_{m_0}e^{\alpha(\phi)-\alpha(\phi_0)}a^{-3}$, which we use for the analysis in this section¹.

In terms of dimensionless scalar field variable ($\tilde{\phi}$), the Friedmann equations and the field equation are:

$$\left(\frac{\dot{a}}{a}\right)^2 = H_0^2\Omega_m a^{-3}e^{C(\tilde{\phi}-\tilde{\phi}_0)} + \frac{\dot{\tilde{\phi}}^2}{12} + \frac{\kappa m_{Pl}^2}{12}\tilde{\phi}^{-n} \quad (3.2)$$

$$\ddot{\tilde{\phi}} + 3H\dot{\tilde{\phi}} + U_{,\tilde{\phi}}(\tilde{\phi}) = -6H_0^2 C\Omega_m a^{-3}e^{C(\tilde{\phi}-\tilde{\phi}_0)}, \quad (3.3)$$

where we have assumed $\alpha(\tilde{\phi})$ to be a linear function of $\tilde{\phi}$, i. e. $\alpha(\tilde{\phi}) = C\tilde{\phi}$, giving $\alpha_{,\tilde{\phi}} = C$. The parameter C is dimensionless and defines the strength of interaction between dark energy and dark matter. In our analysis, we obtain the constraint on C by keeping it as a free parameter with $C \in [-1, 1]$.

3.1 Observational data

We analyze four different observational data sets to constrain the model parameters in the interacting dark sector model. More specifically, we use Hubble parameter measurements (Hz) [54, 55, 57, 60, 84, 85], high redshift HII Galaxy (HIIG) data [62–67], Baryon acoustic oscillation (BAO) data [68–72] and the joint lightcurve analysis (JLA) sample of Type Ia supernovae (SN) observations [73, 86–89].

Hubble Parameter Measurement (H(z)) data: The Hubble parameter measurements (abbreviated as Hz) at different redshifts is an effective tool to constrain the cosmological parameters [54, 57]. Hz observations are useful in constraining the cosmological parameters as it uses the model parameters directly without having an integral term that might obscure or cover valuable information. In the literature, two different techniques are employed to measure the Hubble parameter: a) Differential age method [84] and b) Radial BAO method [85]. In this work, we use the differential age method, where the Hubble rate as a function of redshift is evaluated by using the expression:

$$H(z) = -\frac{1}{(1+z)}\frac{dz}{dt}, \quad (3.4)$$

where t denotes the age of the Universe when the observable photon is emitted. In the differential method, we can obtain a direct estimate of the expansion rate by taking the derivative of redshift with respect to time. Hubble parameter obtained through this method does not depend on the cosmological model but on the age-redshift relation of cosmic chronometers. So very carefully, the selection of passively evolving early galaxies as cosmic chronometers is made depending upon a galaxy's star formation history and its metallicity.

In this work, we consider the Hz data points obtained through the cosmic chronometric technique and use the data points compiled in Ref. [54]. In this compilation, the authors dropped older Hubble parameter estimates from SDSS galaxy clustering [90] and Ly- α forest

¹The constant factor $e^{-\alpha(\phi_0)}$ can be absorbed in ρ_{m_0}

measurement [91] and added new data sets. Out of the 38 data points reported in Ref. [54], in this analysis, we only use 31 independent measurements of the Hubble parameter ($H(z)$). More specifically, we use 9 data points from Ref. [55], 2 points from Ref. [56], 8 points from Ref. [57], 5 points from Ref. [58], 2 points from Ref. [59], 4 points from Ref. [60], and one point from Ref. [61]. Note that the three points reported in Ref. [92] and another three points in Ref. [68] are also used in the BAO observations, hence removed from this data set.

BAO: Baryon Acoustic Oscillations (BAO) are fluctuations in the correlation function of large-scale structures that appear as overdense regions in the distribution of the visible, baryonic matter. This is the consequence of acoustic waves set up in the primordial plasma because of competing forces of radiation pressure and gravity. These acoustic waves travel within the plasma. However, they are frozen at the time of recombination when the plasma cooled down enough to make the cosmos neutral. The distances where the waves stall are imprinted as overdense regions and are used as a standard ruler to measure cosmological distances.

The characteristic angular scale of the acoustic peak is given in terms of sound horizon at drag epoch, $r_s(z_d)$, as $\theta_A = r_s(z_d)/D_V(z)$, where D_V is the effective distance ratio given in terms of angular diameter distance D_A :

$$D_V(z) = \left[(1+z)^2 D_A(z)^2 \frac{cz}{H(z)} \right]^{1/3}, \quad r_s(z_d) = \int_{z_d}^{\infty} \frac{c_s(z') dz'}{H(z')}. \quad (3.5)$$

In order to use the BAO data, the knowledge of the sound horizon scale at the z_d (denoted by r_s) is required as the data is given in terms of $H(z)r_s/r_{s, fid}$, $D_M r_{s, fid}/r_s$, $D_V r_{s, fid}/r_s$, where $r_{s, fid}$ is 147.78 Mpc in [68] and [71], and 148.69 Mpc [70] and the comoving angular diameter distance is given by

$$D_M(z) = (1+z)D_A(z). \quad (3.6)$$

The value of fiducial sound horizon, $r_{s, fid}$ which was calculated by assuming the Λ CDM model and the best fit values of parameters given by Planck-2018 [6], is model dependent, but not to a significant degree. The quantities $D_V r_{s, fid}/r_s$, $D_M r_{s, fid}/r_s$, r_s and $r_{s, fid}$ is given in units of Mpc while $H(z)r_s/r_{s, fid}$ is given in units of $\text{km s}^{-1}\text{Mpc}^{-1}$. We compute r_s using the inverse distance ladder method given in Ref. [93]. In Sec. (IV), we have studied the perturbation evolution in the dark sector interacting model, and in the range $1500 < z < 20$, the evolution is nearly identical to the non-interacting case. Hence, we can use the inverse distance ladder to measure distances, and the Hubble parameter at the corresponding redshifts will be approximately the same for the interacting dark sector model. The BAO data in terms of Acoustic parameter $A(z)$ is defined as [94]:

$$A(z) = \left[\frac{100 D_V(z) \sqrt{(\Omega_m h^2)}}{cz} \right]^{1/3}. \quad (3.7)$$

Thus, the BAO data consists of $A(z)$ and $D_V(z)$ (with associated errors) at different redshifts. The measurement of these distances is a useful tool to constrain cosmological model parameters. The BAO data we use in the analysis lie in the redshift span of $0.106 - 2.36$ and contains 11 points reported in Refs. [68–72]. Among the data we use in the analysis, data points from BOSS DR12 [68] are correlated, and the rest of the data points are uncorrelated. In this work, we assume that the different data sets are independent of each other.

HIIG: The third data set we use is the high redshift HII galaxy (HIIG) observations [62–67]. These observations are new independent cosmological observations that use the correlation

between the Balmer emission line velocity dispersion (σ) and luminosity (L) in HIIG to obtain the distance estimator. This L - σ correlation is given by:

$$\log(L) = \beta \log(\sigma) + \gamma, \quad (3.8)$$

where, γ and β are the intercept and slope, respectively and $\log = \log_{10}$. The tight correlation between the Balmer line luminosity (L) and velocity dispersion (σ) of the emission lines can be used to constrain the cosmological model parameters.

An extinction correction must be made to the observed fluxes to obtain the values of these parameters. We follow the method used in Ref. [62] and assume the extinction law given in Ref. [95]. The resulting value of the intercept and slope are:

$$\beta = 5.022 \pm 0.058, \quad (3.9)$$

$$\gamma = 33.268 \pm 0.083, \quad (3.10)$$

respectively. In our analysis, we use these values of β and γ . The β and γ values are obtained by fitting only the ‘local sample’, i.e. 36 Giant Extragalactic HII Regions for which the authors have distance estimates from Cepheids, and 107 HII galaxies with $z \leq 0.15$. Together the two samples were used to calibrate the L - σ relation and the value of H_0 (cf. Ref. [96, 97]). Using these values in Eq.(3.8), we obtain the luminosity of a HII Galaxy. We then use the luminosity to obtain the distance modulus for that HII Galaxy:

$$\mu_{\text{obs}} = 2.5 \log L - 2.5 \log f - 100.2, \quad (3.11)$$

where f denotes the measured flux of the HIIG, reported in the HIIG observational data along with the error associated with it. We can predict the distance modulus for a given cosmological model by using the theoretical definition:

$$\mu_{\text{th}}(z) = 5 \log D_L(z) + 25, \quad (3.12)$$

where the luminosity distance $D_L(z)$ (in the units of Mpc) is related to the angular size distance $D_A(z)$ via distance duality relation and the transverse comoving distance $D_M(z)$ through $D_L(z) = (1+z)^2 D_A(z) = (1+z) D_M(z)$. The HIIG data we use comprises 153 measurements that span the redshift range of 0.0088 to 2.429, covering a larger redshift range than the BAO data used in this analysis.

SN data (JLA): Type Ia supernovae, which are standardizable candles, is another useful tool to determine the expansion history of the Universe [73, 86–89]. The observable reported in the sample is the distance modulus, which is extracted from light curves by assuming that the intrinsic luminosity on average is the same for Type Ia supernovae with the identical color, shape, and environment, irrespective of the redshift measurement. The standardized distance modulus, obtained by using the following linear empirical relation:

$$\mu^{\text{obs}} = m_B^* + \alpha x_1 - \beta C - M_B. \quad (3.13)$$

Here, m_B^* is the peak magnitude observed in the B-band rest frame, α and β are nuisance parameters, C is the color of supernovae at peak brightness, and x_1 is ‘stretch’ of the light curve. The values of the parameters (m_B, x_1, C) are obtained by fitting supernovae spectral sequence to the photometric data. The parameter M_B , which is the absolute B-band magnitude, depends on the host stellar mass. The theoretical value of the distance modulus μ_{th} is given by Eq. (3.12), which depends on the cosmological model.

By measuring the apparent brightness and comparing it to other candles, one can estimate the distance the photons have traveled, and hence the rate of expansion of the Universe. Our analysis uses the full joint lightcurve analysis (JLA) sample comprising 740 Type Ia Supernovae spanning a redshift range of $z=0.01$ to $z=1.4$. We use the abbreviation ‘SN’ to denote these 740 sample points.

3.2 Data analysis technique

For our analysis, we use the χ^2 minimization technique. Any measurement data contains an observable quantity $X_{\text{obs}}(z_i)$ and its corresponding redshift z_i , along with the error associated with each point σ_i . Here, ‘ i ’ takes the values up to N (number of data points in each observation). We can also estimate these observable quantities theoretically [$X_{\text{th}}(z_i)$] for the models considered in the analysis.

For $H(z)$ data, the observable is the expansion rate, and we consider 31 points obtained using cosmic chronometer, and the χ^2 is defined as:

$$\chi_{\text{H}}^2(\mathbf{p}) = \sum_{i=1}^{31} \frac{[H_{\text{th}}(\mathbf{p}, z_i) - H_{\text{obs}}(z_i)]^2}{\sigma_i^2}, \quad (3.14)$$

where, σ_i is the uncertainty of $H_{\text{obs}}(z_i)$. All these 31 points are independent of each other, and the expansion rate depends on the specific model chosen represented by ‘ \mathbf{p} ’ in the above expression.

For the BAO data points that are correlated (BOSS DR12), χ_{BAO}^2 is given by

$$\chi_{\text{BAO}}^2(\mathbf{p}) = [X_{\text{th}}(\mathbf{p}) - X_{\text{obs}}(z_i)]^T \mathbf{C}^{-1} [X_{\text{th}}(\mathbf{p}) - X_{\text{obs}}(z_i)], \quad (3.15)$$

where superscripts T and -1 denote the transpose and inverse of the matrices, respectively. For the data, we use the covariance matrix \mathbf{C} from Ref. [68].

For HIIG data consisting of 153 measurements, the χ^2 is given by

$$\chi_{\text{HIIG}}^2(\mathbf{p}) = \sum_{i=1}^{153} \frac{[\mu_{\text{th}}(\mathbf{p}, z_i) - \mu_{\text{obs}}(z_i)]^2}{\sigma_i'^2}, \quad (3.16)$$

where σ_i' is the uncertainty of the i_{th} measurement (not to be confused with the velocity dispersion (σ) term in HIIG measurements) and is given by

$$\sigma' = \sqrt{\sigma_{\text{stat}}'^2 + \sigma_{\text{sys}}'^2}. \quad (3.17)$$

σ'_{stat} is the statistical uncertainties and is given by:

$$\sigma_{\text{stat}}'^2 = 6.25 [\sigma_{\log f}^{\prime 2} + \beta^2 \sigma_{\log \sigma}^{\prime 2} + \sigma_{\beta}^{\prime 2} (\log \sigma)^2 + \sigma_{\gamma}^{\prime 2}] + \left(\frac{\partial \mu_{\text{th}}}{\partial z} \right)^2 \sigma_z^{\prime 2}. \quad (3.18)$$

Due to the distance modulus term in the expression, the statistical uncertainty calculated this way is model-dependent. However, when it comes to constraining the cosmological parameters, the model dependence is negligible [98]. In this analysis, we account for the reported systematic uncertainties i. e., $\sigma^2 = \sigma_{\text{stat}}^2 + \sigma_{\text{sys}}^2$.

²In Ref. [99], the authors presented in greater detail a systematic error of ~ 0.25 , taking into account the uncertainties introduced from the size and age of the burst, abundances, and extinction [See also, Ref. [63]].

For the SN data with 740 joint light curves sample, the χ^2 function is:

$$\chi_{\text{SN}}^2(\mathbf{p}) = \sum_{i,j=1}^{740} [\mu_{\text{th}}(\mathbf{p}, z_i) - \mu_{\text{o}}(z_i)] C_{ij}^{-1} [\mu_{\text{th}}(\mathbf{p}, z_j) - \mu_{\text{o}}(z_j)] \quad (3.19)$$

where C_{ij} is the covariance matrix given in Ref. [73].

For the joint analysis (Hz+BAO+HIIG+SN), we obtain the joint likelihood ($e^{-\chi^2}$) by multiplying individual likelihoods such that $\chi^2 = \chi_H^2 + \chi_{\text{BAO}}^2 + \chi_{\text{HIIG}}^2 + \chi_{\text{SN}}^2$. Here, the maximum likelihood corresponds to the minimum value of χ^2 .

3.3 Parameter constraints

Having discussed the data sets and the technique, we can now obtain parameter constraints for the interacting dark sector model discussed at the starting of this section. More specifically, we use the χ^2 technique³ (described in Sec. 3.2) to obtain the 1σ , 2σ , and 3σ confidence regions corresponding to the four data sets for various cosmological parameters used in our dark energy- dark matter interaction model. For a given value of n in the scalar-field potential (3.1), we obtain the constraints on the standard model parameters H_0 , Ω_m , w_0 and the parameter C , which describes the interaction strength in the dark sector.

For the parameter fitting, we use priors that are consistent with the different constraints obtained from various observations. For the Hubble constant, we take the range to be $H_0 = 60 - 80 \text{ km s}^{-1} \text{ Mpc}^{-1}$. In Ref. [52], two of the current authors studied the background evolution of the model for a range of initial conditions and showed that the accelerated attractor solution admitted by the model corresponds to $w = -1$. Thus, in the redshift range $1500 \geq z \geq 0$, $w \geq -1$ satisfy the dominant energy condition [105]. It is important to note that $w < -1$ will lead to the destruction of all the structures [106]. Hence, we use the range $-1 < w_\phi < 1$ and the present-day value of the dark-energy equation of state parameter is set between $-1 \leq w_0 \leq 1$. The non-relativistic matter density is taken to be in the range $0.01 \leq \Omega_m \leq 0.6$, and the interaction strength between dark matter-dark energy is taken to be between $-1 \leq C \leq 1$. These priors are listed in Table 1.

Parameter	Lower Limit	Upper Limit
H_0	60.0	80.0
Ω_m	0.1	0.6
w_0	-1.0	1.0
C	-1.0	1.0

Table 1. Priors used in the analysis of parameter fitting.

Figure 1 contains the constraints on parameters H_0 , interaction strength C , and Ω_m for the four observational data sets. The plots are for $n = 1$ (3.1). Analysis is also done for $n = 2$ and $n = 3$; however, there is no significant change in the parameter constraints. For completeness, in Appendix C, we have presented the results for $n = 2$. The 1σ , 2σ , 3σ contours corresponding to 67%, 95% and 99% confidence regions respectively, are shown in two-dimensional planes in Figure 1. The first, second, and third columns correspond to

³For calculating χ^2 , the Metropolis-Hastings algorithm [100–102] is used to sample the parameter space, and we have modified the MCMC module by Benjamin Audren [103] to constrain the parameters. The convergence of Metropolis-Hastings runs depends on the value of the statistics (R) [104].

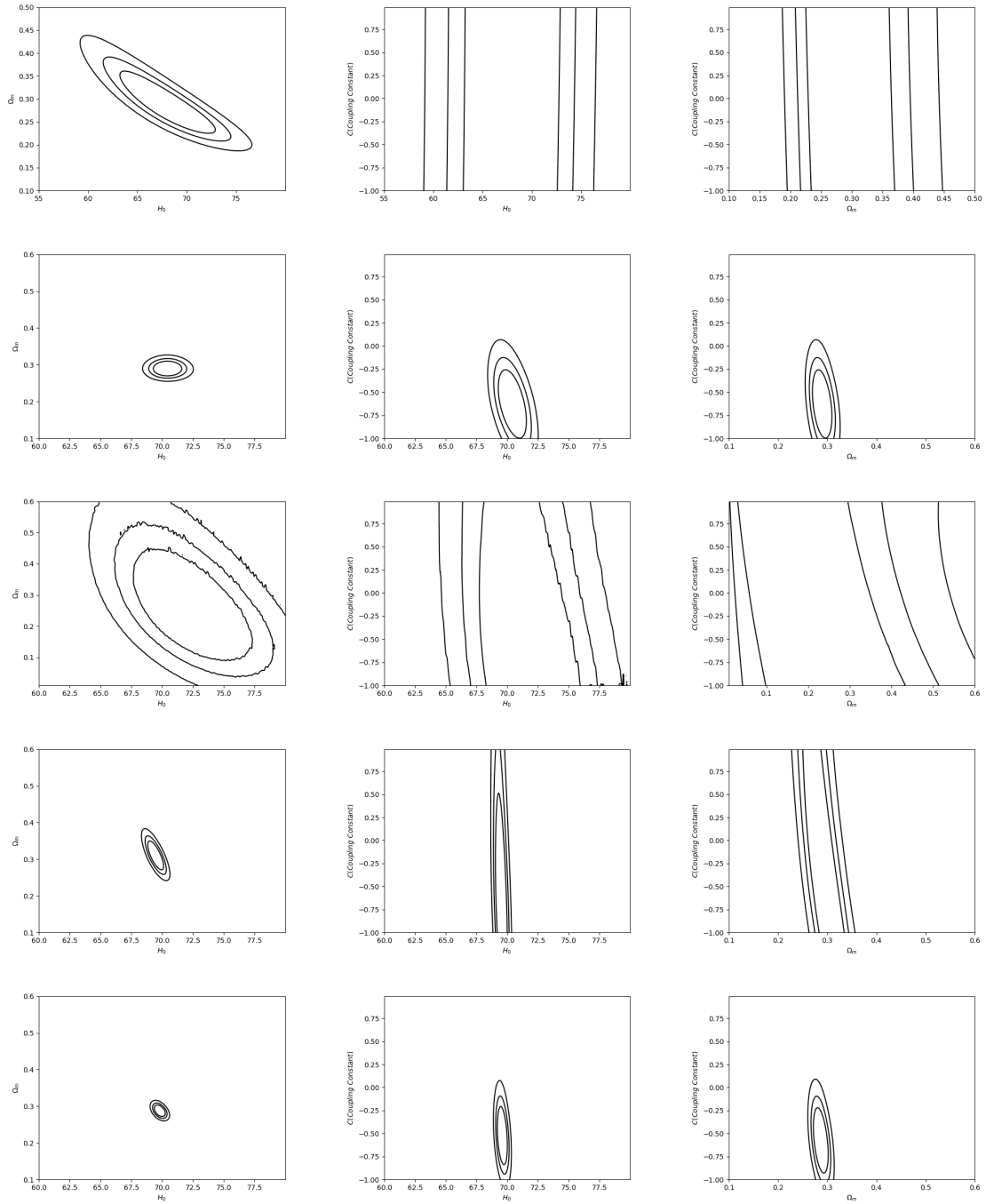


Figure 1. 1,2,3- σ likelihood contours for Hz data (I row), BAO+Hz data (II row), HIIG data (III row), SN+Hz data (IV row) and all four data sets (V row). The two-dimensional contours are obtained by performing marginalization over other parameters.

‘ $H_0 - \Omega_m$ ’, ‘ $H_0 - C$ ’ and ‘ $\Omega_m - C$ ’ planes, respectively. To show these two-dimensional confidence regions, we have marginalized over the other parameters. The two-dimensional confidence regions for standard parameters w_0 and Ω_m are shown in Figure 2. Table 2 contains the best fit values of the parameters. Table 2 contains the allowed range of parameters. In the first row, we show constraints from Hz measurements. In the second row, results from BAO+Hz observations are shown, and the third row represents the confidence contours from HIIG data, while results in the fourth row are from SN+Hz observations. The fifth row shows the constraints obtained from the combination of all the data sets mentioned in section 3.1.

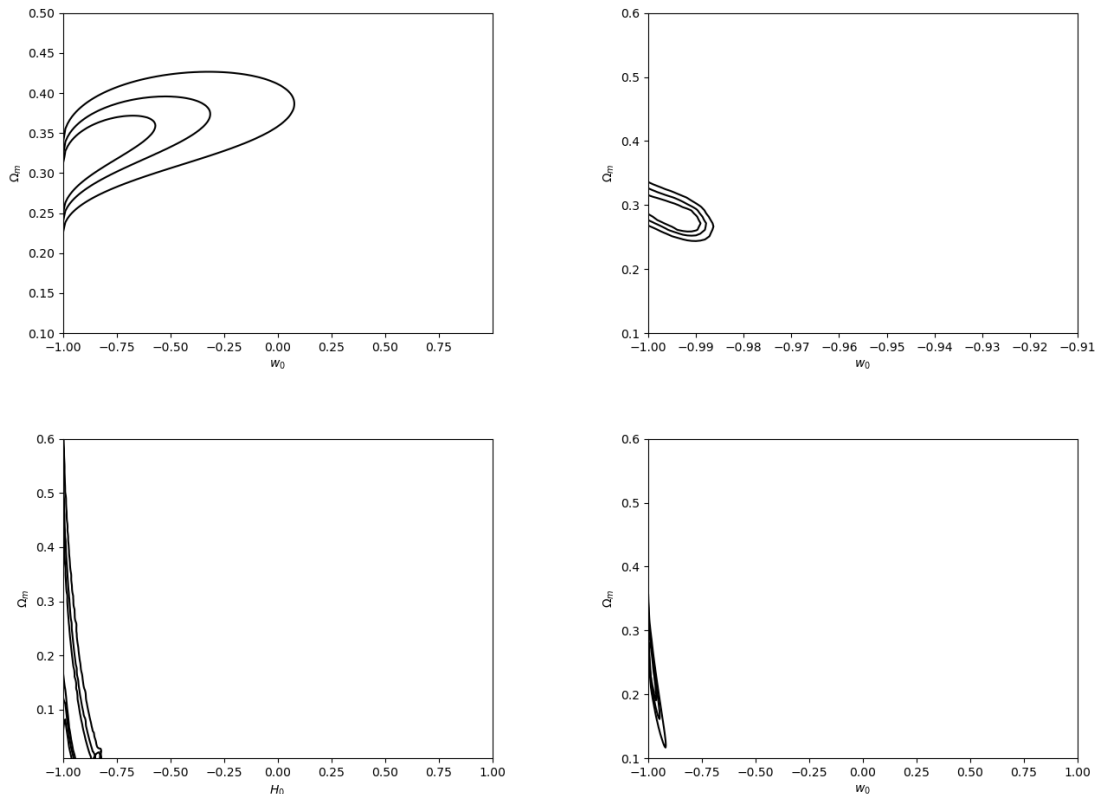


Figure 2. 1,2,3- σ likelihood contours in ‘ w_0 - Ω_m ’ plane. The top row shows constraints from Hz data (left) and BAO+Hz observations (right). The second row shows constraints from HIIG measurements (left) and SN+Hz observations (right).

The key inferences from the Hz data are as follows: First, the minimum value of χ^2 is 18.81 which corresponds to the best fit values of the parameters $H_0 = 69.34 \text{ km s}^{-1} \text{ Mpc}^{-1}$, $\Omega_m = 0.29$, $w_0 = -0.98$ and the interaction strength $C = 0.98$. Second, within the 2σ region, the Hz data allows H_0 to take values between $61.19 - 74.12 \text{ km s}^{-1} \text{ Mpc}^{-1}$ which includes the values reported by Planck [6] and the local measurements [14, 107]. Hence, with Hz observations, the interacting dark sector model is consistent with both of these reported values. Third, the best fit value, as well as the allowed range of non-relativistic density parameter, is also consistent with the constraints reported in the previous studies [6, 14, 107]. Fourth, after marginalizing over parameter w_0 , the data allows the entire range of the coupling parameter (C) considered in the analysis within the 1σ region see Figure 1. However, we also find that if we fix w_0 at a particular value, say $w_0 = -1$, it does not constrain C at all,

Data set	1 σ Confidence	2 σ confidence	3 σ confidence	Best-fit values	χ^2	dof, ν	χ^2_{red}	AIC	BIC
Hz	$64.19 \leq H_0 \leq 72.11$	$61.19 \leq H_0 \leq 74.12$	$59.76 \leq H_0 \leq 75.91$	$H_0=69.34$	18.81	27	0.697	26.81	32.54
	$0.24 \leq \Omega_m \leq 0.34$	$0.21 \leq \Omega_m \leq 0.39$	$0.19 \leq \Omega_m \leq 0.43$	$\Omega_m=0.29$					
	$-1 \leq w_0 \leq -0.67$	$-1 \leq w_0 \leq -0.24$	$-1 \leq w_0 \leq 0.04$	$w_0=-0.989$					
	$-1 \leq C \leq 1$	$-1 \leq C \leq 1$	$-1 \leq C \leq 1$	$C=0.98$					
BAO+Hz	$69.31 \leq H_0 \leq 71.61$	$68.95 \leq H_0 \leq 71.98$	$68.42 \leq H_0 \leq 72.57$	$H_0=70.4$	21.87	37	0.591	29.87	36.72
	$0.269 \leq \Omega_m \leq 0.309$	$0.264 \leq \Omega_m \leq 0.316$	$0.254 \leq \Omega_m \leq 0.32$	$\Omega_m=0.29$					
	$-1 \leq w_0 \leq -0.989$	$-1 \leq w_0 \leq -0.987$	$-1 \leq w_0 \leq -0.985$	$w_0=-0.997$					
	$-1 \leq C \leq -0.261$	$-1 \leq C \leq -0.132$	$-1 \leq C \leq 0.067$	$C=-0.63$					
HIIG	$67.78 \leq H_0 \leq 77.2$	$66.29 \leq H_0 \leq 78.9$	$64.07 \leq H_0 \leq 80$	$H_0=72.49$	226.79	149	1.522	234.79	246.91
	$0.091 \leq \Omega_m \leq 0.447$	$0.041 \leq \Omega_m \leq 0.53$	$0.01 \leq \Omega_m \leq 0.6$	$\Omega_m=0.25$					
	$-1 \leq w_0 \leq -0.87$	$-1 \leq w_0 \leq -0.84$	$-1 \leq w_0 \leq -0.81$	$w_0=-0.92$					
	$-1 \leq C \leq 1$	$-1 \leq C \leq 1$	$-1 \leq C \leq 1$	$C=-0.94$					
SN+Hz	$69.18 \leq H_0 \leq 70.02$	$69.06 \leq H_0 \leq 70.19$	$68.87 \leq H_0 \leq 70.36$	$H_0=69.51$	737.21	767	0.961	745.21	763.8
	$0.25 \leq \Omega_m \leq 0.33$	$0.24 \leq \Omega_m \leq 0.34$	$0.22 \leq \Omega_m \leq 0.35$	$\Omega_m=0.31$					
	$-1 \leq w_0 \leq -0.97$	$-1 \leq w_0 \leq -0.93$	$-1 \leq w_0 \leq -0.9$	$w_0=-1$					
	$-1 \leq C \leq -0.51$	$-1 \leq C \leq 1$	$-1 \leq C \leq 1$	$C=-0.69$					
Hz+BAO+HIIG+SN	$69.27 \leq H_0 \leq 70.08$	$69.07 \leq H_0 \leq 70.19$	$68.83 \leq H_0 \leq 70.59$	$H_0=69.79$	968.322	930	1.041	976.332	995.67
	$0.27 \leq \Omega_m \leq 0.303$	$0.266 \leq \Omega_m \leq 0.308$	$0.26 \leq \Omega_m \leq 0.316$	$\Omega_m=0.29$	(739.014)	(777)	(0.951)	(747.014)	(766.372)
	$-1 \leq w_0 \leq -0.99$	$-1 \leq w_0 \leq -0.987$	$-1 \leq w_0 \leq -0.985$	$w_0=-0.99$					
	$-0.83 \leq C \leq -0.21$	$-0.93 \leq C \leq -0.099$	$-1 \leq C \leq 0.087$	$C=-0.52$					

Table 2. Confidence limits, best fit values of parameters, AIC, BIC and χ^2 values from various data sets for interacting dark sector cosmology. The values in the brackets in the last row correspond to the analysis of combined data set excluding the HIIG data.

but if we move away from Λ CDM like scenarios at present, and consider $w_0 \geq -1$ then we start getting a limit on C as well. As the value of w_0 moves away from -1 towards 1 , the constraints on C becomes tighter (cf. Figure 3). Fifth, from Figure 2, we see that the Hz data does not provide a lower limit on w_0 ; however, an upper limit of -0.67 within 1σ and $w_0=0.04$ within 3σ region is allowed showing that this particular model does not allow for a non-accelerating universe within 1σ region. Also, Hz is the only observation that allows for a non-accelerating universe within the 3σ region. The allowed range for w_0 is the widest compared to the other three observations considered in the analysis. The Hz measurements constrain Ω_m to take values within a range of $0.19 - 0.43$ for 3σ confidence level, which is very wide compared to the ones obtained from BAO+Hz and SN+Hz data sets.

The key inferences from BAO+Hz data are as follows: First, the minimum value of χ^2 is 21.87 which corresponds to the best fit values of parameters giving $H_0 = 70.4 \text{ km s}^{-1}\text{Mpc}^{-1}$, $\Omega_m = 0.29$, $w_0 = -0.997$ and the interaction strength is $C = -0.63$. Second, within 1σ region, BAO+Hz data allows H_0 to take a very small range given by $69.31 - 71.61 \text{ km s}^{-1}\text{Mpc}^{-1}$ which lies between the value of H_0 reported by Planck [6] and the local probes [14, 107]. Third, the best fit value of the non-relativistic matter density parameter is $\Omega_m = 0.29$. The allowed range within the 3σ region is very narrow and consistent with the constraints reported in the previous studies [6, 14, 107]. Fourth, within 1σ , BAO+Hz data also constrains the interaction strength C within the range of -1.0 to -0.261 (cf. Figure 1) and between -1 to 0.067 corresponding to 99% confidence region. Thus, BAO+Hz data prefers negative values of C . Here again, we find that if we fix w_0 at a particular value, say $w_0 = -1$, the allowed range is narrower than when w_0 was a free parameter. And if we move away from Λ CDM-like scenarios at present, and consider $w_0 \geq -1$, then the upper limit on C starts getting lower as the contours shift to the negative regions on C . As we change w_0 from -1 towards 1 , the constraints on C become tighter as in Hz data, and we find that the BAO+Hz data prefers negative values of C . Fifth, from Figure 2, we see that the BAO+Hz data provide very small range on w_0 for 1σ , 2σ region and within 3σ region Λ CDM case is allowed. Therefore, the BAO+Hz observational data do not allow for a non-accelerating universe and prefer a Λ CDM like scenario. It also provides the tightest constraints for the model parameters out of all the observational data-sets considered.

The key inferences from HIIG data are as follows: First, the minimum value of χ^2 is 226.79 which corresponds to the best fit parameters $H_0 = 72.49 \text{ km s}^{-1}\text{Mpc}^{-1}$, $\Omega_m = 0.25$, $w_0 = -0.92$ and the interaction strength is $C = -0.94$. Second, HIIG data allows H_0 to take values in the range $67.78 - 77.2 \text{ km s}^{-1}\text{Mpc}^{-1}$ within 1σ region. The best fit value for the model indicates the preference for the value of H_0 reported by local measurements [14, 107]. However, the interacting dark sector model is also consistent with the H_0 value reported in Ref. [6] within 3σ region. Third, the best fit value of the non-relativistic density parameter preferred by HIIG data is smaller than the value reported in the previous studies [6, 14, 107]. Fourth, similar to Hz data, HIIG data allows the entire range of coupling parameter (C) within the 1σ region, see Figure 1. Here again, we have marginalized over parameter w_0 . We also found that if we fix w_0 at a particular value and consider $w_0 \geq -1$, then we see a slight shift in contour which is almost insignificant in changing $w = -1$ to $w \sim -0.985$. Fifth, from Figure 2, we see that the HIIG data does not provide a lower limit on w_0 . Still, an upper limit of -0.81 within the 3σ region is allowed, showing that similar to BAO+Hz data, this particular model does not allow for a non-accelerating universe within 3σ region. The results are consistent with the Λ CDM model. These observations' constraints on Ω_m give the widest range amongst all data sets considered in the analysis.

The key inferences from SN+Hz data are as follows: First, the minimum value of χ^2 is 737.21 which corresponds to the best fit values of the parameters $H_0 = 69.51 \text{ km s}^{-1}\text{Mpc}^{-1}$, $\Omega_m = 0.31$, $w_0 = -1.0$ and $C = -1$. Second, the SN+Hz data allows H_0 to take values between $\sim 69.18 - 70.02 \text{ km s}^{-1}\text{Mpc}^{-1}$ within 1σ region, which lies between the values reported by Planck-2018 [6] and the local H_0 measurements [14, 107]. Interestingly, it provides a very narrow range for H_0 and, hence, the interacting dark sector model can potentially alleviate the H_0 tension.

Third, the best fit value, as well as the allowed range of non-relativistic density parameter, is also consistent with the constraints reported in previous studies [6]. Fourth, like Hz data, SN+Hz data also allows the entire range of the interaction strength (C) within the 3σ region. However, within 1σ region, it constrains C to be less than 0.5, (cf. Figure 1). Here again, we have marginalized over parameter w_0 . We find that like other data sets, SN+Hz also prefers negative values of interaction strength.

Fifth, from Figure 2, we see that the SN+Hz data does not provide a lower limit on w_0 . However, within the 1σ , there is an upper limit of -0.97 , and $w_0 = -0.9$ within the 3σ region. Thus, the analysis shows that a non-accelerating universe is not allowed. The allowed values of Ω_m are very narrow and consistent with previous studies. This model is also consistent with the Λ CDM model. We have done the analysis with Pantheon compilation of SN for some specific values of model parameters H_0 , Ω_m , and C , and we get similar results (cf. appendix B).

The key inferences from the combined data are as follows: First, the minimum value of χ^2 is 968.332, which corresponds to the best fit values of the parameters are $H_0 = 69.79 \text{ km s}^{-1}\text{Mpc}^{-1}$, $\Omega_m = 0.29$, $w_0 = -0.99$ and the interaction strength is $C = -0.52$. Second, the Hz+BAO+HIIG+SN data allows H_0 to take values between $\sim 69.27 - 70.08 \text{ km s}^{-1}\text{Mpc}^{-1}$ within 1σ region, which lies between the values reported by Planck-2018 [6] and the local probes [14, 107]. It provides a very narrow range for H_0 within the 3σ confidence region. Therefore, this dark sector interaction model puts very narrow constraints on model parameters with the joint analysis. Third, the best fit value, as well as the allowed range of non-relativistic density parameter, is also consistent with a narrow range of allowed values with $0.316 \geq \Omega_m \geq 0.26$ within 3σ region, and these constraints are consistent with the ones reported in previous studies [6, 14]. Fourth, we get a very narrow range for the coupling parameter for the joint analysis, C , which restricts it to take values only within -0.83 to -0.21 for 1σ and from -1 to 0.087 for 3σ confidence regions, see Figure 1. In the joint analysis, the constraints are driven by the BAO observation, which has the most constraining capacity, followed by SN, Hz, and HIIG observations. Like the individual cases, if we fix w_0 at a particular value, say $w_0 = -1$, the combination data gives a slightly narrower range. If we move away from Λ CDM-like scenarios at present, for $w_0 \geq -1$, there is a preference for negative values of C .

Fifth, from Figure 2, we see that the combined data does not provide a lower limit on w_0 . However, within 1σ , we get the upper limit of -0.993 and $w_0 = -0.99$ within 3σ region. This again shows that the model does not allow for a non-accelerating universe and constrains w_0 to a value close to -1 , and is consistent with the Λ CDM model.

In Figure 3, instead of marginalizing w_0 , we assume a value of w_0 within 3σ allowed range reported in this work and see the change in the $H_0 - C$ plane. The first row is obtained for Hz data, and the value of w_0 considered are -1 , -0.6 , and -0.1 (left, middle, and right plots, respectively). In the second, third, fourth, and fifth rows, the results correspond to BAO+Hz, HIIG, SN+Hz, and combined analysis, respectively. For the left, middle and

right plots, respectively, we fix w_0 at -1 , -0.99 , and -0.985 . For Hz measurements, we see a significant change in the constraints as w_0 changes from -1 to -0.1 , and we start getting constraints on C . But for BAO+Hz, HIIG, SN+Hz, and combined case, there is a slight shift in contours in contours when w_0 is varied from $w_0=-1$ to -0.985 (within 3σ range).

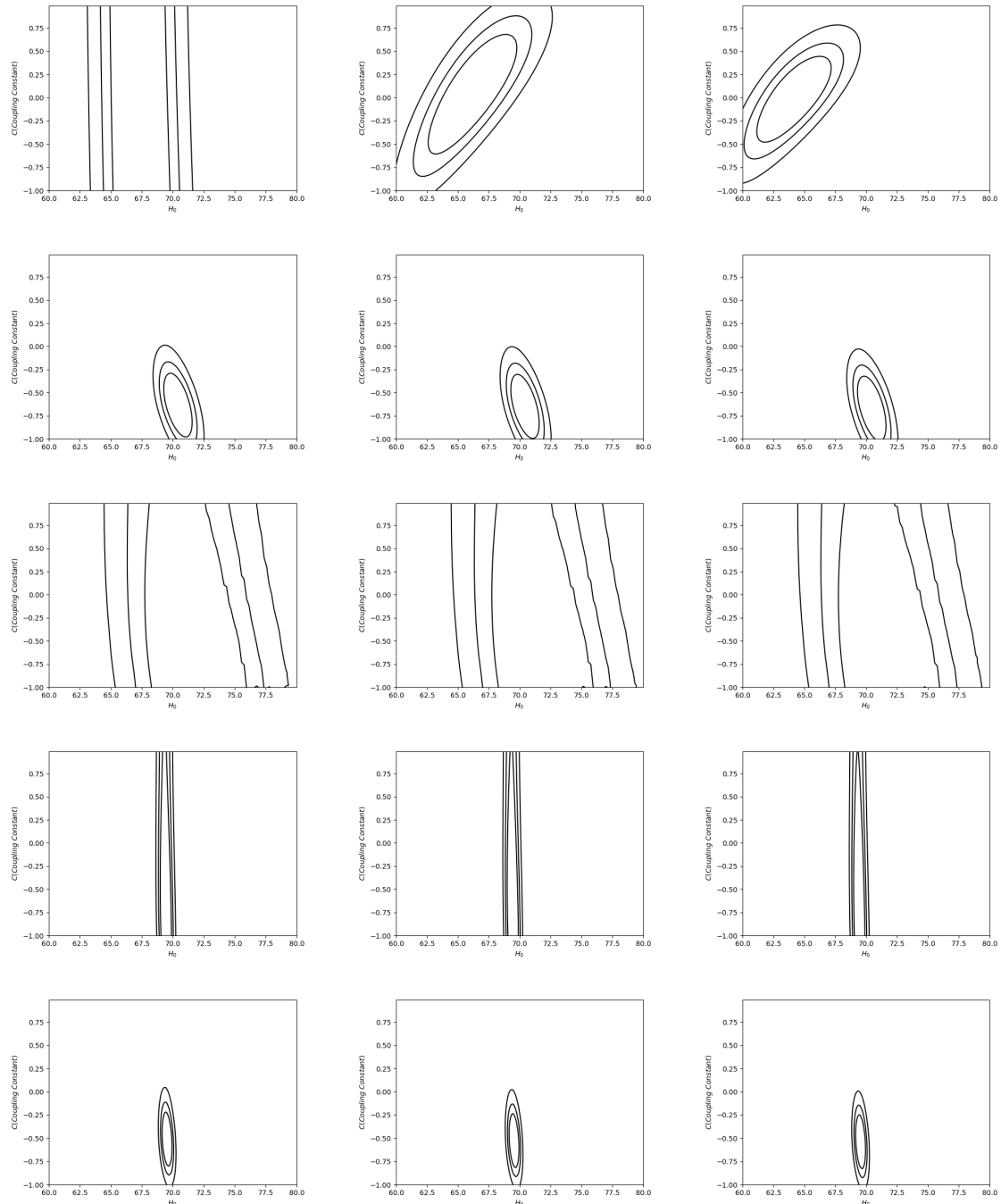


Figure 3. 1,2,3- σ likelihood contours in ‘ $H_0 - C$ ’ plane for different values of w_0 . Plots show constraints from Hz data (I row), BAO+Hz (II row), HIIG data (III row), SN+Hz (IV row) and all four data sets (V row). The left, middle and right plots correspond to different w_0 values. For $H(z)$ data we choose $w_0 = [-1, -0.6, -0.1]$ and for the remaining data sets, we choose $w_0 = [-1, -0.99, -0.985]$.

Thus, from these analyses, we make the following conclusions:

1. All the observational data sets considered constrain H_0 to be close to $70 \text{ km s}^{-1} \text{ Mpc}^{-1}$. The dark sector interaction model puts very narrow constraints on the model parameters.
2. The constraints on Ω_m obtained from various data sets are consistent with each other.
3. The constraints on w_0 are consistent with the Λ CDM model, and only Hz data allows for a non-accelerating universe.
4. All data sets, except Hz, prefer negative value for the interaction strength (C).
5. We have also done the combined analysis excluding the HIIG data and found that the best fit values and constraints are approximately the same. The results corresponding to this analysis are given in the brackets in the last row of Table 2.
6. Our analysis shows no significant difference in the best-fit values for different values of n (specifically, for $n = 1$ and $n = 2$ (See Appendix C)). However, we notice that the allowed range of cosmological parameters (H_0, Ω_m, w_0) increases for HIIG as we go from $n = 1$ to $n = 2$. In the case of interaction parameter C , Hz shows no significant change, HIIG data allows a wider range, whereas for BAO+Hz and SN+Hz case, the contour shifts lower, thereby giving a smaller value for the upper limit of C .

The reduced χ^2 values for the interacting dark sector model we have considered is closer to one (except for HIIG and combined data sets) compared to Λ CDM and w CDM models. (see Appendix A). Thus, our analysis points to the fact that there is a strong degeneracy between the interacting and non-interacting dark sector models with respect to these low-redshift background observations. In the next section, we explicitly show that the first-order perturbations can break the degeneracy between these two scenarios.

4 Evolution of the scalar perturbations and predictions of the model

In the previous sections, we obtained the constraints on the various model parameters based on the observational data related to the background evolution of the Universe. From these constraints, it is apparent that we need to go beyond the background observations to distinguish between non-interacting and interacting dark sector models. This section looks at the evolution of first-order perturbations for negative value for the interaction strength (C).

The perturbed FRW metric in the Newtonian gauge given by [8]:

$$g_{00} = -(1 + 2\Phi), \quad g_{0i} = 0, \quad g_{ij} = a^2(1 - 2\Psi)\delta_{ij}, \quad (4.1)$$

where $\Phi \equiv \Phi(t, x, y, z)$ and $\Psi \equiv \Psi(t, x, y, z)$ are the Bardeen Potentials.

We obtain the evolution of three perturbed quantities, which are relevant to three different cosmological observations:

1. Structure formation: $\delta_m(t, x, y, z) \equiv \frac{\delta\rho_m(t, x, y, z)}{\rho_m(t)}$
2. Weak lensing : $\Phi + \Psi$
3. Integrated Sachs-Wolfe (ISW) effect: $\Phi' + \Psi'$

where δ_m is the density perturbation of dark matter fluid. We study the evolution of these perturbed quantities for various length scales specified by the wavenumber k .

To analyze the difference in the evolution of the scalar perturbations in dark sector interactions compared to standard cosmology, we study the following quantities:

$$\Delta\delta_m = \delta_{m_i} - \delta_{m_{ni}}, \quad \Delta\delta_{m_{rel}} = \frac{\delta_{m_i} - \delta_{m_{ni}}}{\delta_{m_{ni}}} = \frac{\Delta\delta_m}{\delta_{m_{ni}}} \quad (4.2a)$$

$$\Delta\Phi = \Phi_i - \Phi_{ni}, \quad \Delta\Phi_{rel} = \frac{\Phi_i - \Phi_{ni}}{\Phi_{ni}} = \frac{\Delta\Phi}{\Phi_{ni}} \quad (4.2b)$$

$$\Delta\Phi' = \Phi'_i - \Phi'_{ni}, \quad \Delta\Phi'_{rel} = \frac{\Phi'_i - \Phi'_{ni}}{\Phi'_{ni}} = \frac{\Delta\Phi'}{\Phi'_{ni}} \quad (4.2c)$$

where the subscripts i and ni denote the interacting and non-interacting scenarios, respectively.

The perturbed interaction term in the fluid description is given by

$$\delta Q^{(F)} = -(\delta\rho_m - 3\delta p_m)\alpha_{,\phi}(\bar{\phi})\dot{\bar{\phi}} - (\bar{p}_m - 3\bar{p}_m) \left[\alpha_{,\phi\phi}(\bar{\phi})\dot{\bar{\phi}}\delta\phi + \alpha_{,\phi}(\bar{\phi})\dot{\delta\phi} \right] \quad (4.3)$$

In appendix B of Ref. [52], the authors obtained the scalar perturbations equations for the interacting dark sector model. We rewrite these equations in terms of the following dimensionless variables:

$$x = \sqrt{\frac{8\pi}{6}} \frac{\dot{\phi}}{H m_{Pl}}, \quad y = \sqrt{\frac{8\pi}{3}} \frac{\sqrt{U}}{H m_{Pl}}, \quad \lambda = -\frac{m_{Pl}}{\sqrt{8\pi}} \frac{U_{,\phi}}{U}, \quad \Gamma = \frac{UU_{,\phi\phi}}{U^2_{,\phi}} \\ \alpha = \alpha(\phi), \quad \beta = -\frac{m_{Pl}}{\sqrt{8\pi}} \frac{\alpha_{,\phi}}{\alpha}, \quad \gamma = \frac{\alpha\alpha_{,\phi\phi}}{\alpha^2_{,\phi}} \quad (4.4)$$

In terms of these dimensionless variables, the scalar perturbation equations are [52]:

$$\delta\phi'' + \left[\frac{3}{2} (y^2 - x^2 - \omega\Omega_m + 1) - 3\sqrt{6}\alpha\beta x \left(c_s^2 - \frac{1}{3} \right) \right] \delta\phi' \\ + \left[-9\beta \left(\Omega_m \gamma \left(\omega - \frac{1}{3} \right) \beta - y^2 \left(c_s^2 - \frac{1}{3} \right) \lambda \right) \alpha + 3\Gamma\lambda^2 y^2 + \frac{k^2}{a^2 H^2} \right] \delta\phi \\ + \left[-18\sqrt{2}\alpha\beta \left(c_s^2 - \frac{1}{3} \right) - 8\sqrt{3}x \right] \Phi' \\ - 18\sqrt{2} \left[\alpha\beta \left(\left(c_s^2 - \frac{1}{3} \right) \left(y^2 + \frac{k^2}{3a^2 H^2} \right) + (c_s^2 - \omega) \right) + \frac{\lambda y^2}{3} \right] \Phi = 0 \quad (4.5)$$

$$\Phi'' + \frac{3}{2} \left[y^2 - x^2 - \Omega_m \omega + 2c_s^2 + \frac{5}{3} \right] \Phi' + 3 \left[c_s^2 \left(\frac{k^2}{3a^2 H^2} - x^2 + 1 \right) - \Omega_m \omega + y^2 \right] \Phi \\ + \frac{\sqrt{3}x}{2} (c_s^2 - 1) \delta\phi' - \frac{3\sqrt{2}\lambda y^2}{4} (c_s^2 + 1) \delta\phi = 0 \quad (4.6)$$

$$\delta' + 3(\omega - c_s^2)(\sqrt{6}\alpha\beta x - 1)\delta + \frac{2}{3} \frac{k^2}{a^2 H^2 \Omega_m} \Phi + \left(-3\omega - 3 + \frac{k^2}{a^2 H^2 \Omega_m} \right) \Phi' \\ - \frac{1}{\sqrt{2}} \alpha\beta(3\omega - 1)\delta\phi' + \sqrt{3} \left[\alpha\beta^2\gamma(3\omega - 1) - \frac{1}{9} \frac{k^2}{a^2 H^2 \Omega_m} \right] x\delta\phi = 0 \quad (4.7)$$

where ω and c_s denote the equation of state and sound speed of the dark matter fluid, respectively. We solve these equations for the redshift range $0 \leq z \lesssim 1500$. Hence for the analysis in this section, we include the contributions of radiation, dark matter, and dark energy to the total energy density of the Universe. The calculations are done in the rest frame of the pressureless dark matter fluid, for which $\omega = c_s^2 = 0$ (cf. Appendix E). As mentioned in Sec 2, this analysis is done for $U(\phi) \sim 1/\phi$ and $\alpha(\phi) \sim \phi$. Analysis is also done for $n = 2$, however, the results are not sensitive to n . For completeness, in Appendix D, we have presented the results for $n = 2$.

To understand the effect of the interaction between dark energy and dark matter on the perturbed quantities, we define scaled interaction function δq :

$$\delta q = \frac{\delta Q}{H^3 M_{Pl}^2}. \quad (4.8)$$

Figure 4 is the plot of δq as a function of number of e-foldings (N) for different k values.

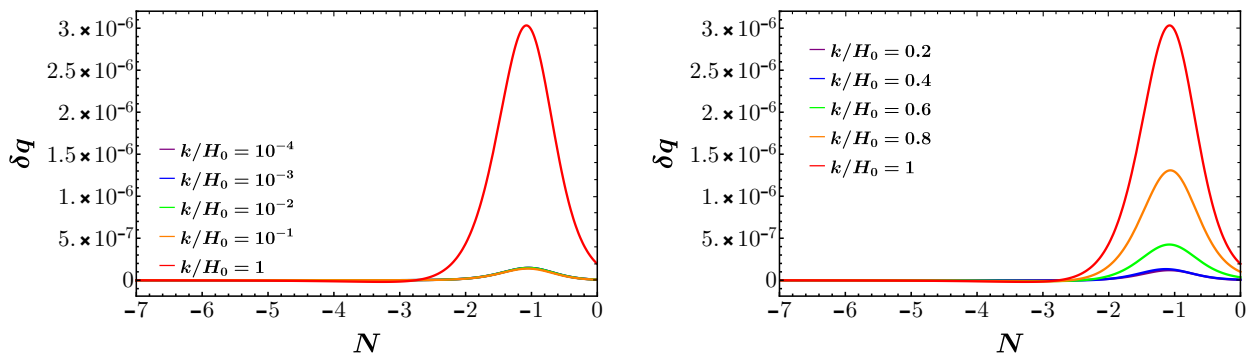


Figure 4. Evolution of δq as a function of N for different values of k , with $C = -0.6$.

Since this forms the basis of the rest of the analysis, we would like to stress the following points: First, we see that the interaction function peaks around $N \sim -1$ ($z \sim 1.5 - 2.5$), and the interaction increases with increasing values of k . Second, since the interaction in the dark sector is a local interaction, the effect of the interaction should be least at the largest length scales (smallest k), and this is what we see from the plots. In other words, the interaction strength introduces a new length scale in the dynamics and leads to a preference for the growth of perturbations in certain length scales. We will see this feature for all the three quantities δ_m , $\Phi + \Psi$ and $\Phi' + \Psi'$.

In the following subsections, we obtain the evolution of the perturbed quantities relevant to the upcoming cosmological observations and determine the constraints to distinguish the interacting dark sector model from standard cosmology.

4.1 Structure formation

Over the last few decades, the three-dimensional distribution of galaxies is available due to many surveys. With the redshift measurement of millions of galaxies, there are two key conclusions: First, if we smoothen the distribution on the largest scales, it approaches a homogeneous distribution consistent with the FRW model. Second, in the smaller scales, there are overdense regions (clusters) and underdense regions (voids); around 10 Mpc, the RMS density-fluctuation amplitude is of the order unity. Since the interaction function, δq

increases with increasing values of k , we can expect that the cold matter density perturbations in our model may have a different profile compared to standard cosmology.

Hence, first we look at the evolution of the matter density perturbation δ_m . More specifically, δ_m , $\Delta\delta_m$ and $\Delta\delta_{m_{rel}}$ defined in Eq. (4.2a).

To gain a physical understanding of the effect of the interaction term on the evolution of the perturbed quantities, we consider an approximation in which the perturbed interaction term is switched off ($\delta q = 0$). The right panel in Figure 5 contains the evolution of $\Delta\delta_m$ with and without this approximation. Dashed lines refer to the evolution with the approximation, and the solid lines refer to the full evolution (without any approximation).

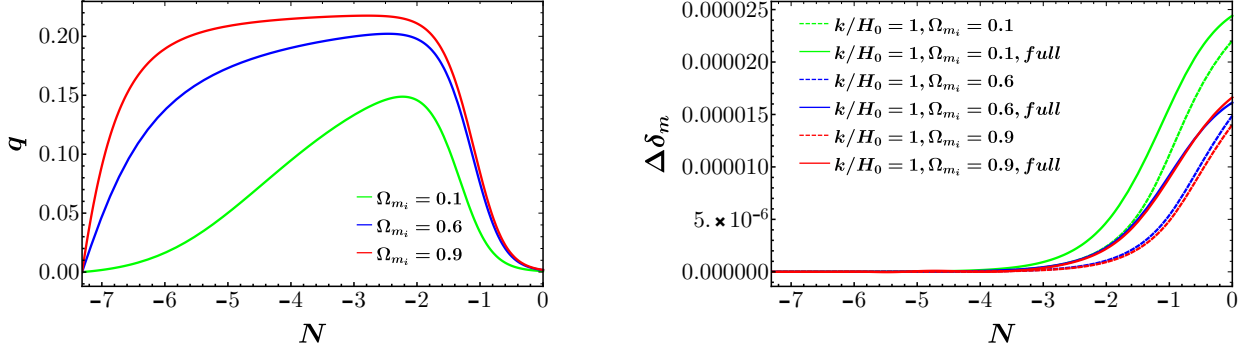


Figure 5. Evolution of q (left panel) and $\Delta\delta_m$ (right panel) as a function of N with $C = -0.6$.

The background interaction term $q \equiv \alpha\beta x\Omega_m$ determines the rate of growth of δ_m . Larger the initial value of Ω_m , the value of q increases at an earlier epoch and stays at a higher value till $N \sim -2$ ($z \sim 7.4$). This behaviour can be seen in the left panel of Figure 5. The right panel of Figure 5 contains the evolution of $\Delta\delta_m$. Here, we see that the growth of δ_m is suppressed for the larger initial values of Ω_m . A better analytical understanding will shine a light on the role of Q^F in the evolution of the perturbed quantities.

In the rest of this section, we numerically evolve the Eqs. 4.5 and obtain the evolution of the perturbed quantities.

Figures 6 and 7 [8 and 9] contain plots of δ_m [$\Delta\delta_m$, $\Delta\delta_{m_{rel}}$] as a function of N for different length scales in interacting and non-interacting scenarios.

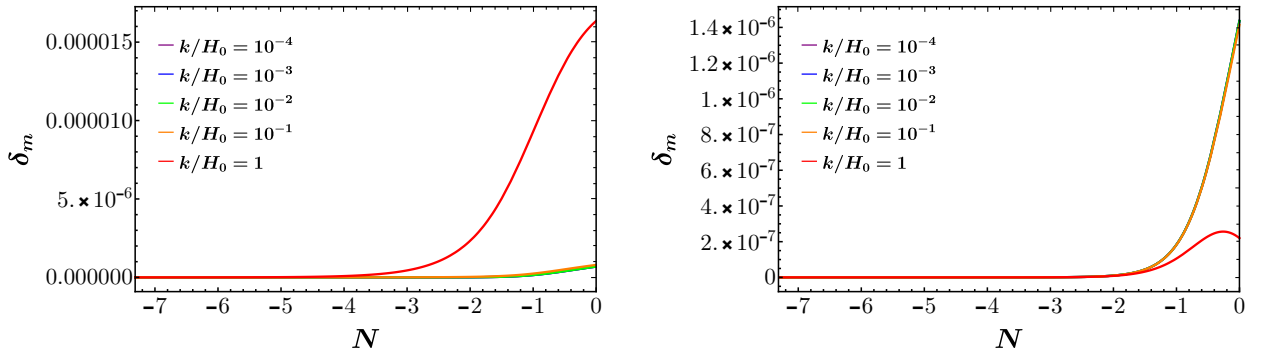


Figure 6. Evolution of δ_m as a function of N . Left: $C = -0.6$, Right: $C = 0$.

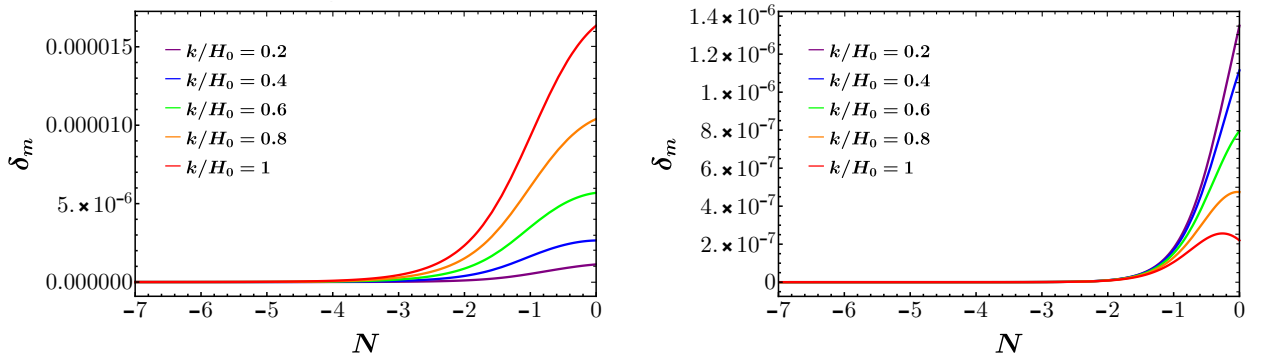


Figure 7. Evolution of δ_m as a function of N . Left: $C = -0.6$, Right: $C = 0$.

From these plots, we infer the following: First, the difference in the evolution of δ_m between the interacting and non-interacting scenarios is significant after $N \sim -3$. Second, this difference increases with the increase in the value of the wavenumber k . This means that the interaction has a more significant effect on the evolution of the scalar perturbations in the smaller length scales (large values of k) than the larger length scales (smaller values of k). Third, these deviations become significant for $z \sim 10 - 20$ and lie in the epoch of reionization. During this epoch, a predominantly neutral intergalactic medium was ionized by the emergence of the first luminous sources. Before the reionization epoch, the formation and evolution of structure were dominated by dark matter alone. However, the interacting dark sector leads to the exchange of density perturbations at smaller length scales. This indicates that it will be possible to detect the signatures of dark energy - dark matter interaction in large-scale structure observations. This provides a possible way to detect the signatures of dark sector interaction in the existing and upcoming cosmological observations like Euclid satellite [108], GMRT [109], SKA [110] and LOFAR [111].

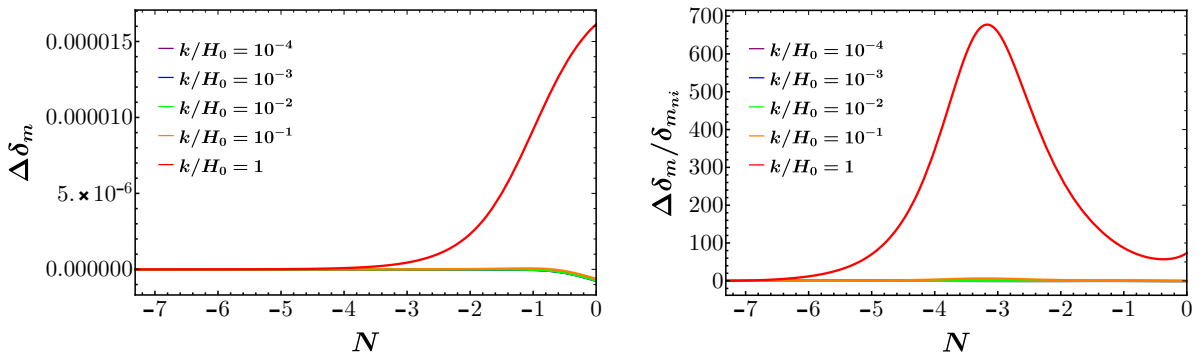


Figure 8. Evolution of $\Delta\delta_m$ (left), $\Delta\delta_m/\delta_{m,ni}$ (right) as a function of N .

4.2 Weak gravitational lensing

The matter content of the Universe is dominated by dark matter. Most of the cosmological observations to study the matter distribution in the Universe depend on the observations of the luminous matter, which gives us little information regarding the total mass distribution in

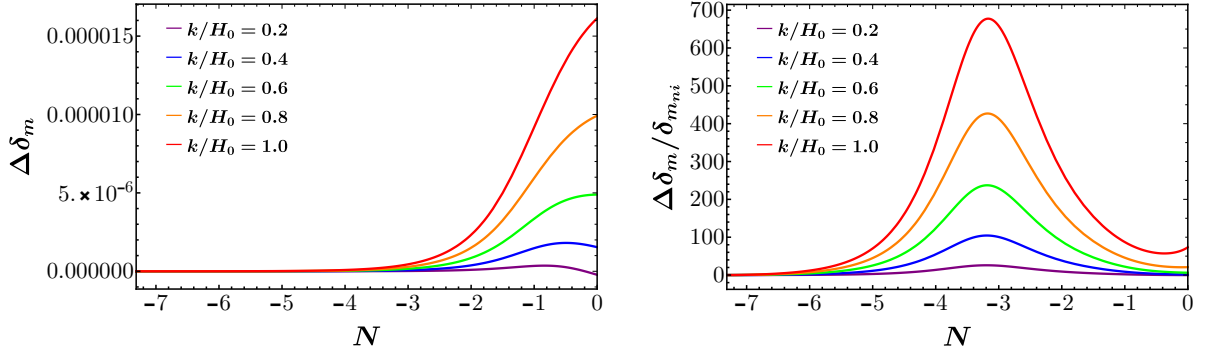


Figure 9. Evolution of $\Delta\delta_m$ (left), $\Delta\delta_m/\delta_{m,ni}$ (right) as a function of N .

the Universe. Gravitational lensing provides important information regarding the total mass distribution in the Universe, as it is independent of the nature of the matter and its interaction with electromagnetic radiation. Hence, weak gravitational lensing holds enormous promise as it can reveal the distribution of dark matter independently of any assumptions about its nature. The quantity $\Phi + \Psi$ determines the geodesic of a photon, which affects the weak gravitational lensing [8]. Like the standard cosmology, for the dark-sector interacting model considered here, $\Phi(t, x, y, z) = \Psi(t, x, y, z)$. Hence, it is sufficient to study the evolution of Φ to distinguish the dark sector model from standard cosmology.

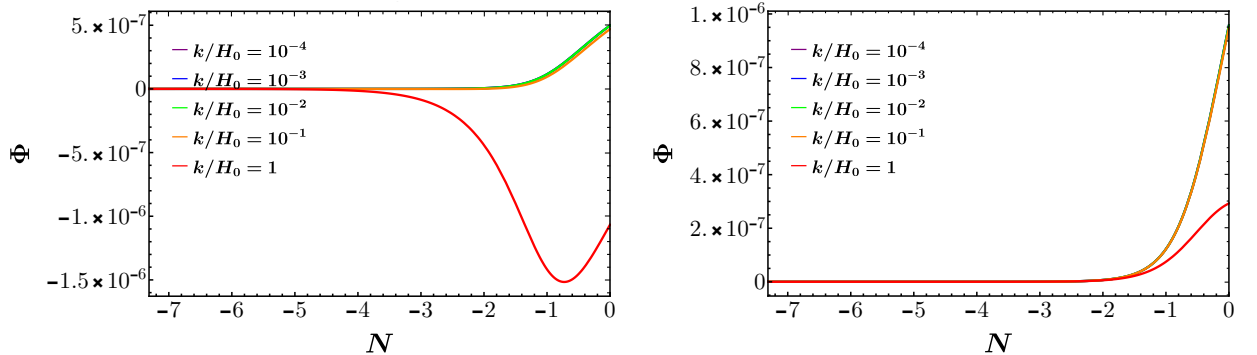


Figure 10. Evolution of Φ as a function of N . Left: $C = -0.6$, Right: $C = 0$.

To study the signatures of the interacting dark sector, we look at the evolution of scalar metric perturbation Φ for different length scales starting from $z \sim 1500$. To analyze the difference in the evolution of Φ in the two scenarios, we also look at $\Delta\Phi$ and $\Delta\Phi_{rel}$. Figures 10 and 11 contain plots of Φ as a function of N for different length scales in interacting and non-interacting scenarios. Evolution of $\Delta\Phi$ and $\Delta\Phi_{rel}$ as a function of N are plotted in Figures 12 and 13.

From the evolution of these quantities, we see that starting from the same initial conditions at $z \sim 1500$, the evolution of Φ begins to show the effect of dark energy - dark matter interaction at about $N \sim -3$. This effect becomes even more prominent towards the lower redshifts $z < 5$. By looking at the k -dependence of the evolution, this effect is enhanced at lower length scales. This means that the interaction has a larger effect on the evolution of

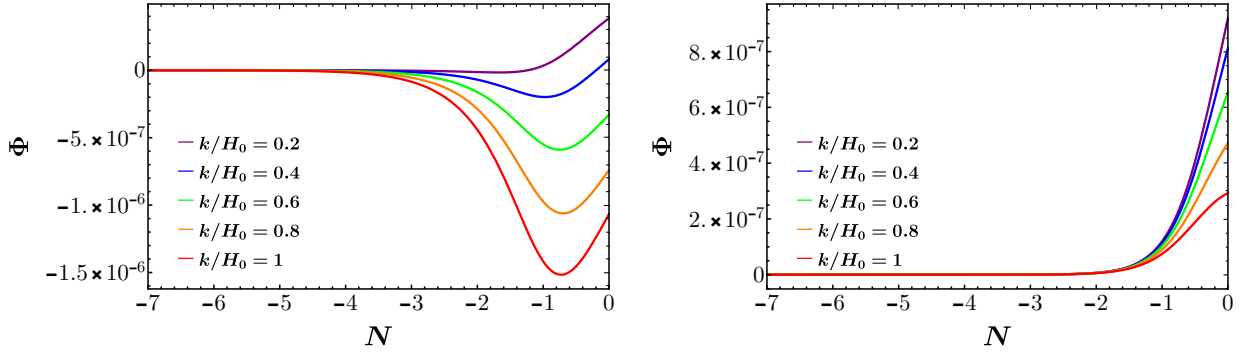


Figure 11. Evolution of Φ as a function of N . Left: $C = -0.6$, Right: $C = 0$.

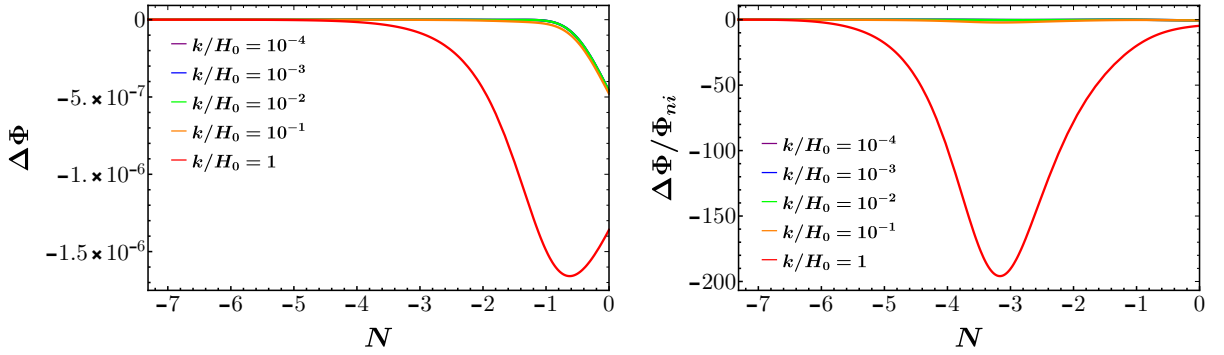


Figure 12. Evolution of $\Delta\Phi$ (left), $\Delta\Phi/\Phi_{ni}$ (right) as a function of N .

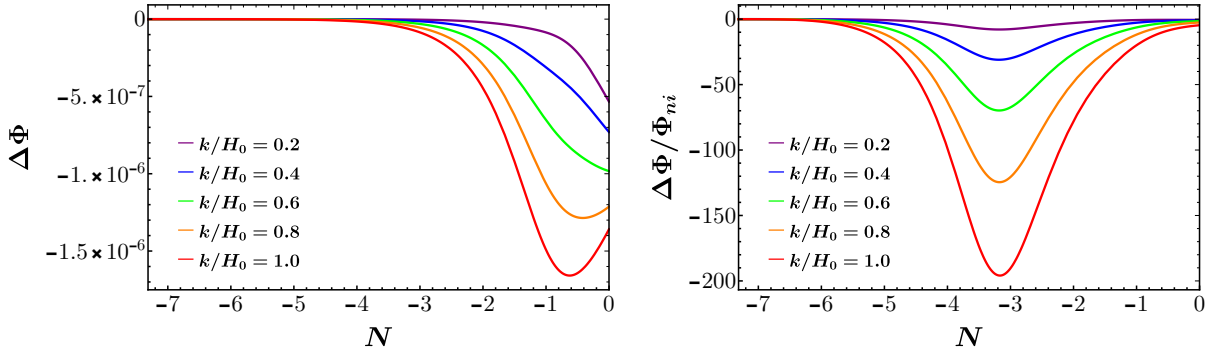


Figure 13. Evolution of $\Delta\Phi$ (left), $\Delta\Phi/\Phi_{ni}$ (right) as a function of N .

the scalar perturbations in the smaller length scales (large values of k) than the larger length scales (smaller values of k). Thus, this indicates that observations of weak lensing can help us potentially distinguish between interacting and non-interacting scenarios and potentially provide a way to resolve the tension between Planck-2018 and KiDS-450, KiDS-1000 [112, 113] in the $\sigma_8 - \Omega_m$ plane.

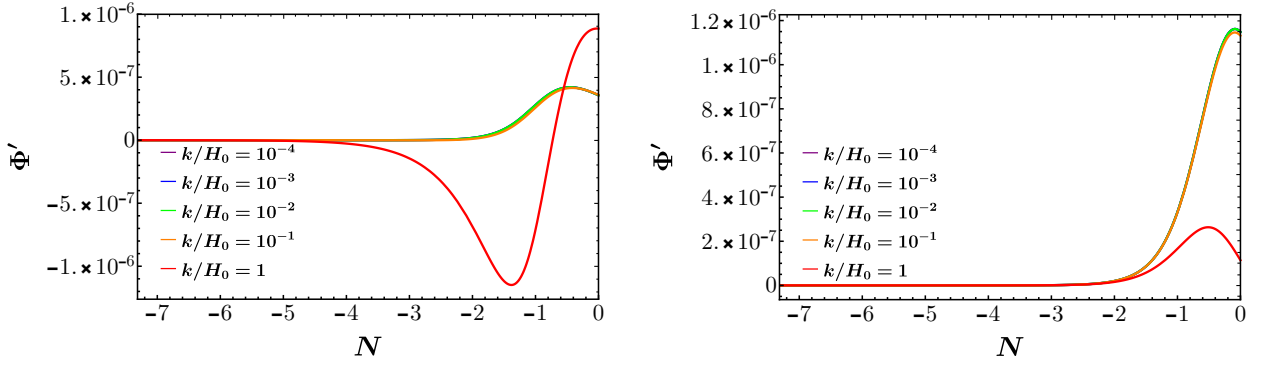


Figure 14. Evolution of Φ' as a function of N . Left: $C = -0.6$, Right: $C = 0$.

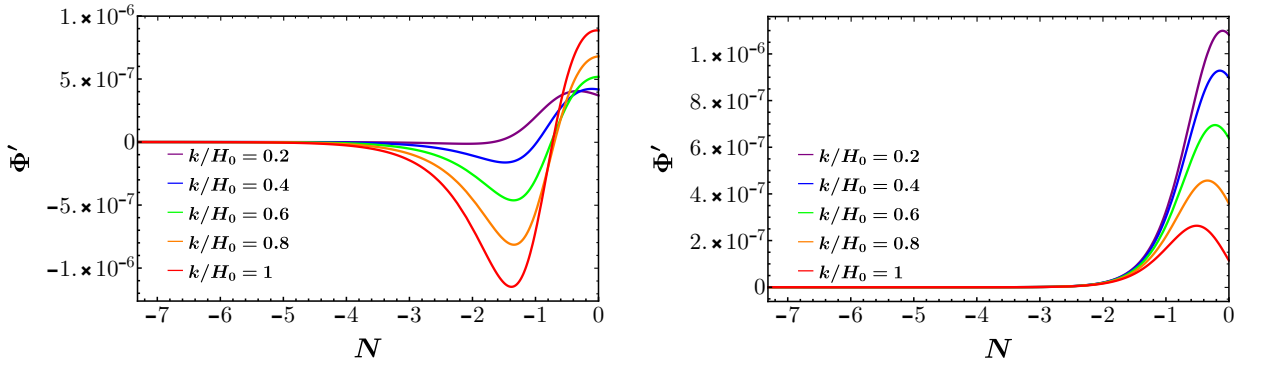


Figure 15. Evolution of Φ' as a function of N . Left: $C = -0.6$, Right: $C = 0$.

4.3 Integrated Sachs-Wolfe effect

The integrated Sachs-Wolfe (ISW) effect is a secondary anisotropy of the cosmic microwave background (CMB), which arises because of the variation in the cosmic gravitational potential between local observers and the surface of the last scattering [114]. The ISW effect is related to the rate of change of $(\Phi + \Psi)$ w.r.t. conformal time (η) [10]. While weak gravitational lensing is determined by the spatial dependence of the metric scalar perturbation Φ , the ISW effect provides valuable information about the time evolution of the same, especially in the late accelerating Universe. Even though its detectability is weaker than weak lensing, it is a powerful tool to study the underlying cosmology. It can be detected using the cross-correlation between the observational data on CMB and large-scale structures. In the flat Λ CDM model, detection of the ISW signal provides direct detection of dark energy [115].

Since the Bardeen potential Φ evolve differently in the interacting and non-interacting scenarios, this change should potentially change the temperature fluctuations of the CMB photons. Figures 14 and 15 contain plots of Φ' as a function of N for different length scales in interacting and non-interacting scenarios. Evolution of $\Delta\Phi'$ and $\Delta\Phi'_{rel}$ as a function of N are plotted in Figures 16 and 17.

Like δ_m and Φ , we see that the difference in the evolution of Φ' in these two scenarios becomes significant at $N \sim -3$. Consistent with the fact that the first-order interaction term is larger at the smaller length scales, the difference in the evolution of Φ' in the interacting and

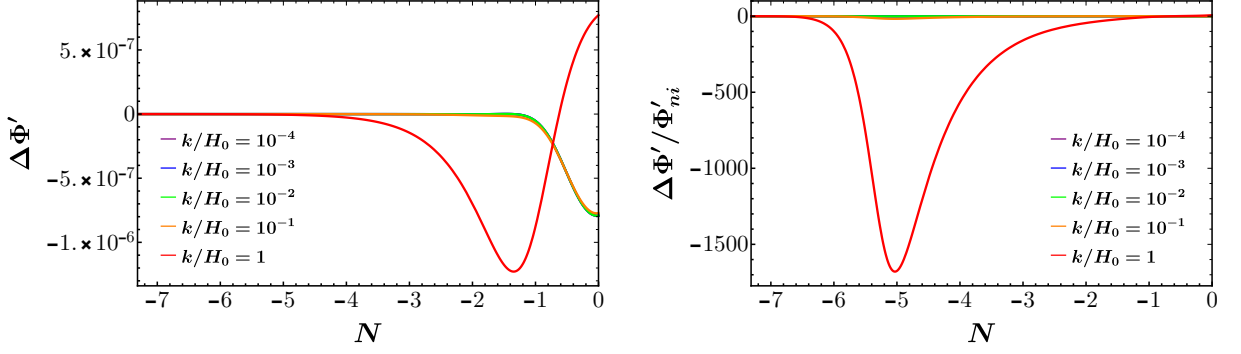


Figure 16. Evolution of $\Delta\Phi'$ (left), $\Delta\Phi'/\Phi'_{ni}$ (right) as a function of N .

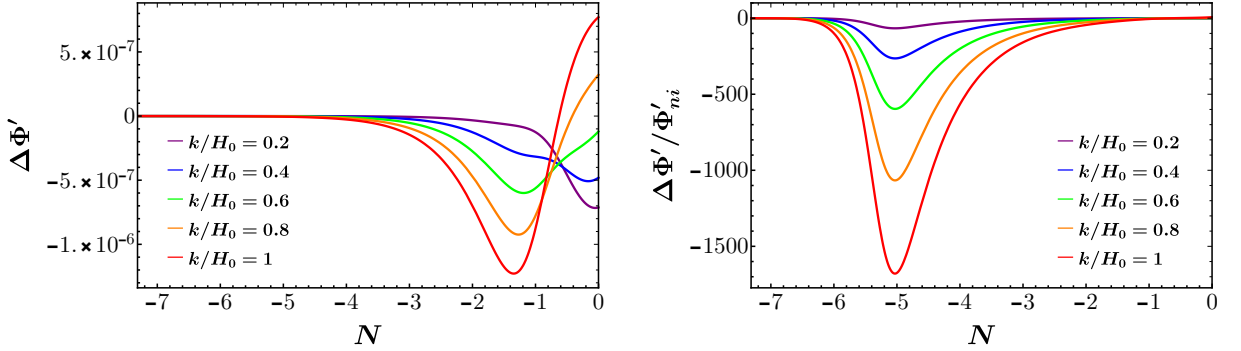


Figure 17. Evolution of $\Delta\Phi'$ (left), $\Delta\Phi'/\Phi'_{ni}$ (right) as a function of N .

non-interacting scenarios is enhanced for larger values of k . This indicates that observations on the ISW effect can detect or constrain dark energy and dark matter interaction.

5 Conclusions

In Ref. [52] two of the current authors found a mapping between phenomenological models of the dark-energy dark matter coupling functions Q from a consistent classical field theory. We showed that the mapping holds both at the background and first-order perturbations level. In this work we used this interacting field theory framework for a specific scalar field potential $U(\phi) \sim 1/\phi^n$ and linear interaction function $\alpha(\phi) \sim \phi$. We analyzed the background cosmological evolution in this model and obtained the model parameters from cosmological observations. We evolved the perturbed equations in the redshift range $1500 \gtrsim z \geq 0$ and obtained testable predictions of the model with future cosmological observations.

Constraints from observations: We obtained constraints for the model parameters from four observational data sets — Hubble parameter measurements, baryon acoustic oscillation observation, high- z HII galaxy measurements, and Type Ia supernovae observations. For numerical analysis, we rewrote the evolution equations in terms of dimensionless variables. Using the χ^2 minimization technique, we obtained the constraints on H_0 , Ω_m , w_0 , and the interaction strength C .

The key conclusions of the analysis for $n = 1$ ($U(\phi) \sim \phi^{-1}$) case are: (i) All the four data sets constrain the value of H_0 to be close to $70 \text{ km s}^{-1}\text{Mpc}^{-1}$. BAO+Hz and SN+Hz

observations provide the tightest constraints, followed by HIIG and Hz measurements. (ii) When a combined analysis of all four data sets is performed, the constraints are impacted by BAO and SN observations the most, and the allowed range for H_0 becomes even narrower. (iii) The constraints on Ω_m obtained from various data sets are consistent with each other, and BAO+Hz provides the smallest allowed range, which drives the limit for combined analysis, followed by SN + Hz, Hz, and then HIIG data. (iv) When it comes to constraining w_0 , all the observations are consistent with the Λ CDM model, and only Hz data allows for a non-accelerating universe. (v) As for the constraints on C , we find that only BAO+Hz data constrains C within 3σ confidence region, and hence, when analysis with a combination of the data sets is performed, the allowed values of C is influenced by BAO+Hz data the most. We also find that, except for Hz measurements, all the three data sets show a preference for a negative value C (cf. Table 2). The Hz data is nearly insensitive to the sign and value of C within the considered range. (vi) Our analysis points to the fact that there is a strong degeneracy between the interacting and non-interacting dark sector models with respect to these low-redshift background observations.

The key conclusions of the analysis for $n = 2$ ($U(\phi) \sim \phi^{-2}$) case are: (i) Constraints from the Hz data set do not change significantly. For other data sets, there is a slight shift in the contours. (ii) The observations prefer slightly higher values of Ω_m , the contours from Hz-data shift towards higher values of Ω_m . HIIG data allows a significantly larger range of Ω_m compared to $n = 1$. For SN+Hz observations, there is no significant change in the lower range but the upper limit on Ω_m shifts slightly higher. For BAO+Hz data, the change in the allowed range of Ω_m is insignificant. (iii) For H_0 , the change is not noticeable when we go from $U(\phi) \sim \phi^{-1}$ to ϕ^{-2} . For w_0 , there is no noticeable change from Hz data, but the allowed ranges increase when the $n = 1$ is changed to $n = 2$ for BAO+Hz, HIIG, and SN+Hz observations. (iv) The constraints on coupling parameter C change significantly when n changes. For $n = 2$, constraints on C from Hz do not show much change. Still, for BAO+Hz and SN+Hz data, we get upper limits on C , and the contours shift towards negative values of C , showing their preference for a negative value of interaction strength. We can also see this in constraints obtained from the combination of data sets. All the observations are consistent with $C = -1$, but BAO+Hz and SN+Hz observations do not agree with $C = 1$ within 1σ confidence regions for $n = 2$ case.

Our analysis shows no significant difference in the best-fit values for different values of n (specifically, for $n = 1$ $n = 2$ (See Appendix C)). However, we notice that the allowed range of cosmological parameters (H_0 , Ω_m , w_0) increases for HIIG as we go from $n = 1$ to $n = 2$. In the case of interaction parameter C , Hz shows no significant change, HIIG data allows a wider range, whereas for BAO+Hz and SN+Hz case, the contour shifts lower, thereby giving a smaller value for the upper limit of C .

Distinguishing dark sector interacting model from standard cosmology: As we have shown, there is a strong degeneracy between the interacting and non-interacting dark sector models with respect to these background observations. To distinguish between the two scenarios, we looked at the evolution of the scalar perturbations in the interacting dark sector model. We considered a inverse potential $U(\phi) \sim 1/\phi$ and a linear interaction function $\alpha(\phi) \sim \phi$ with negative values of interaction strength C . We evolved three perturbed quantities (δ_m , Φ , Φ') from last scattering surface to present epoch ($1500 \lesssim z \leq 0$). These three perturbed quantities are related to structure formation, weak gravitational lensing, and the ISW effect, respectively.

The density perturbation δ_m grows faster in the interacting scenarios, especially at the

lower length scales. The difference in the evolution becomes significant for $z < 20$, for all length scales, and the difference peaks at smaller redshift values $z < 5$. This means that cosmological observations related to the formation of large-scale structures can potentially detect the signatures of dark matter - dark energy interaction. We see a similar trend in the evolution of Φ and Φ' . This indicates an interaction between dark energy and dark matter will be reflected on the observational data on weak gravitational lensing and ISW effect. We get a similar behaviour for inverse-square potential $U(\phi) \propto 1/\phi^2$. The evolution of the perturbations in the interacting dark sector also differs from the ones in modified gravity models like $f(R)$ gravity, which describes the late-time acceleration of the Universe [116]. It was shown that, in the case of $f(R)$ models, the identity $\Phi = \Psi$ does not hold, and the evolution of perturbations are monotonic. As we have shown in this work, for a class of interacting dark sector models, the evolution is more complicated due to the interaction between dark energy and dark matter. Hence these models can potentially be distinguished using future observations.

It is interesting to note that all the perturbed quantities are significant for $z \sim 10 - 20$ and lie in the epoch of reionization. During this epoch, a predominantly neutral intergalactic medium was ionized by the emergence of the first luminous sources. Before the reionization epoch, the formation and evolution of structure were dominated by dark matter alone. However, the interacting dark sector leads to the exchange of density perturbations at smaller length scales. This indicates that it is possible to distinguish these models from the observations at the epoch of reionization.

We have shown that the interacting dark sector model is consistent with the low-redshift background observations and obtained the parameter constraints. The constraints on the dark energy-dark matter interaction model parameters can be used as priors in future studies. We have not addressed the issue of the tension in the $\sigma_8 - \Omega_m$ plane between Planck and cosmic shear experiments [112]. We plan to address this in future work.

Currently, we are looking to obtain the constraints on the model from the evolution of the perturbations using the relevant observational data sets. It will also be interesting to look at the observational consequences of the difference in the evolution of the density perturbation. Since interaction is higher for the smaller length scales, it can significantly affect the evolution of the mass distribution of the binary black holes detected by the gravitational wave observations [117].

6 Acknowledgements

We thank T. Padmanabhan for fruitful discussions. We thank Ana Luisa Gonzalez-Moran for providing Gordon extinction corrected HIIG measurements and useful information related to the measurements (Ref. [96, 97]). JPJ is supported by CSIR Senior Research Fellowship, India. The work is partially supported by the ISRO-Respond grant.

A Best fit values: Λ CDM, w CDM, and interacting dark sector models

In the tables below, we present the *reduced chi-square* values (χ_{red}^2) and the best fit values of the parameters for the simple Λ CDM model and w CDM model compared to the interacting dark sector model.

As we can see, χ_{red}^2 values for the interacting dark sector model we have considered is closer to one (except for HIIG and combined data sets) compared to Λ CDM and w CDM

Observations	H_0	Ω_m	χ_{red}^2
Hz	68.19	0.29	0.652
BAO+Hz	68.52	0.28	0.567
HIIG	72.41	0.259	1.509
SN+Hz	69.8	0.29	0.959
All combined	69.69	0.29	1.039

Observations	H_0	Ω_m	w_0	χ_{red}^2
Hz	70.09	0.28	-1.13	0.673
BAO+Hz	67.34	0.28	-1.03	0.578
HIIG	71.43	0.25	-0.89	1.514
SN+Hz	69.89	0.29	-1.01	0.9599
All combined	70.01	0.28	-1.03	1.040

Table 3. The best fit values of the parameters obtained for Λ CDM model (left panel) and w CDM model (right panel).

Observations	H_0	Ω_m	C	w_0	χ_{red}^2
Hz	69.34	0.29	0.98	-0.989	0.697
BAO+Hz	70.4	0.29	-0.63	-0.997	0.591
HIIG	72.49	0.25	-0.94	-0.92	1.522
SN+Hz	69.51	0.31	-0.69	-1.0	0.961
All combined	69.79	0.29	-0.52	-0.99	1.041

Table 4. The best fit values of the parameters obtained for the dark-energy dark-matter interaction model.

models. In the analysis for HIIG observations, we have used $\sigma = \sigma_{stat}$; therefore, we get a higher χ_{red}^2 . See Ref. [99], where the authors present in greater detail that there is a systematic error of ~ 0.25 . If we include it in the analysis, we will get $\chi_{red}^2 \sim 1$ [62]. Looking at the χ_{red}^2 values, we see that there is a strong degeneracy between the interacting and non-interacting dark sector models with respect to these low-redshift background observations.

Observations	AIC			BIC		
	Λ CDM	w CDM	DEDM	Λ CDM	w CDM	DEDM
Hz	22.93	24.87	26.81	25.798	29.192	32.545
BAO+Hz	26.12	27.99	29.87	29.547	33.131	36.724
HIIG	231.87	233.12	234.79	237.93	242.211	246.911
SN+Hz	741.82	743.21	745.21	751.03	757.03	763.63
All combined	972.57	974.449	976.322	982.248	988.967	995.656

Table 5. AIC and BIC for different models.

The introduction of new parameters often gives a better fit for the data, irrespective of the relevance of the parameter. Therefore, to select which model is better regardless of the number of free parameters, some information criteria are used to penalize additional parameters in the analysis. We use the [Akaike information criterion \(AIC\)](#) [118] and the [Bayesian information criterion \(BIC\)](#) [119] which are defined as $AIC = -2 \ln \mathcal{L} + 2k = \chi_{min}^2 + 2k$ and $BIC = -2 \ln \mathcal{L} + k \ln N = \chi_{min}^2 + k \ln N$. Here, \mathcal{L} and χ_{min} denote the maximum likelihood and minimum χ value for a model, respectively, k denotes the number of parameters of the model, and N denotes the number of data points in the observations.

From the above table, we infer that the interacting dark sector model can provide a good fit for the observations while not being favoured over the Λ CDM model w.r.t. AIC. However, our model is strongly disfavoured w.r.t. BIC for the supernovae data.

B Comparing the parameter constraints from JLA and Pantheon data sets

In this appendix we obtain the constraints on our model parameter for the Pantheon compilation of type Ia Supernovae for fixing values of Ω_m , H_0 and C . We also compare these results with the constraints from JLA in Sec. 3.3.

In Fig. 18, the blue contours correspond to the pantheon data and the red contours are for JLA data by setting $w_0 = -1$. The top row consists of plots of Ω_m vs H_0 for two different values of C . The left plot is for $C = -1$ and the right plot is for $C = -0.5$. The bottom row (left plot) the constraints are in $H_0 - C$ plane by setting $\Omega_m = 0.27$. The bottom row (right plot) the constraints are in $\Omega_m - C$ plane by setting $H_0 = 70 \text{ km s}^{-1} \text{ Mpc}$.

We find that the best fit values of the parameters are the approximately the same from Pantheon and JLA data. However, Pantheon data provides smaller range of parameters. By fixing w_0 , we find that both the data allow the entire range of the interaction strength C .

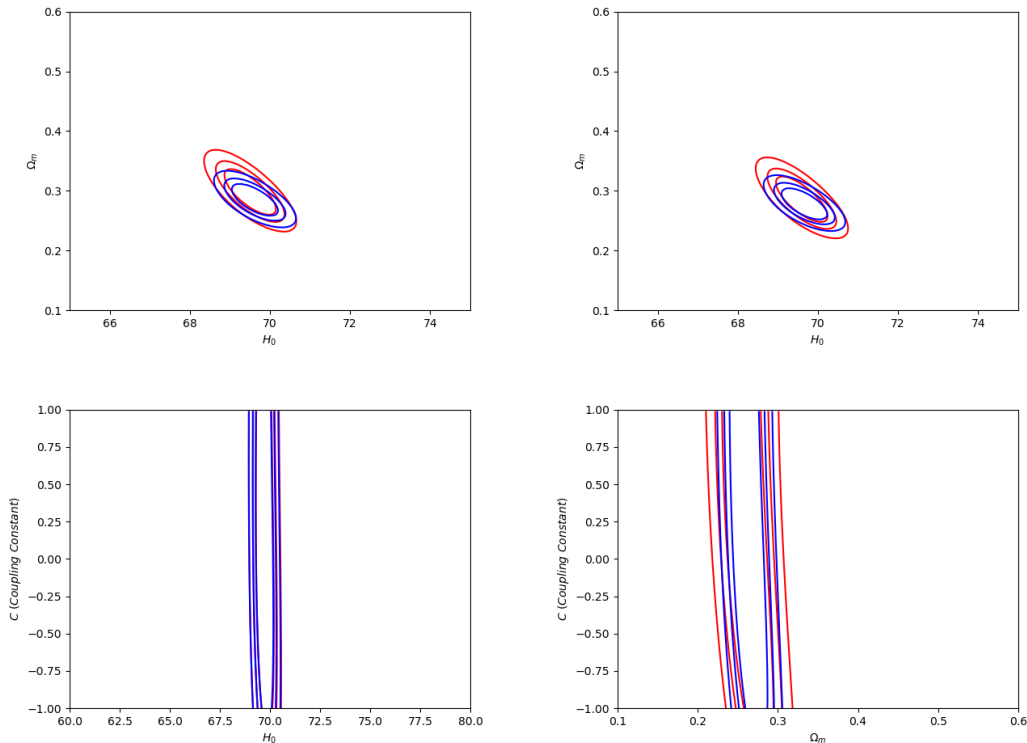


Figure 18. The figure represents 1σ , 2σ and 3σ contours obtained from JLA compilation (red contours) of Type Ia supernovae and from Pantheon data (blue contours). The left figure in the first row shows constraints obtained in $H_0 - \Omega_m$ plane for $C = -1$ and $w_0 = -1$, the right figure in the first row shows results in $H_0 - \Omega_m$ plane for $C = -0.5$ and $w_0 = -1$ from the two SN compilation data sets. The left plot in second row shows constraints in $H_0 - C$ plane for $\Omega_m = 0.27$ and $w_0 = -1$ and the right plot shows confidence contours in $\Omega_m - C$ plane for $H_0 = 70 \text{ km s}^{-1} \text{ Mpc}^{-1}$ and $w_0 = -1$ from SN observations.

C Parameter constraints for $U(\phi) \sim 1/\phi^2$

For completeness, in this Appendix, we present the constraints for $n = 2$ in the quintessence potential (3.1). Note that in Section 3.3, we presented the detailed analysis for $n = 1$. As mentioned earlier, the parameter constraints are roughly the same for $n = 1$ and $n = 2$. Figures 19 and 20 contain the constraints on parameters H_0 , interaction strength C , and Ω_m for the four observational data sets — Hz, BAO, HIIG, and SN.

Here are the key inferences from Figures 19 and 20: (i) For $n = 2$, the constraints on H_0 , w_0 and C obtained from the data sets are almost same as for $n = 1$. (ii) From Hz data, the minimum value of χ^2 is 18.77 which corresponds to the best fit values of the parameters are $H_0 = 69.37 \text{ km s}^{-1}\text{Mpc}^{-1}$, $\Omega_m = 0.29$, $w_0 = -0.98$ and the interaction strength is $C = 0.98$. (iii) For BAO+Hz data, when it comes to the interaction strength C , the preference for negative value is more evident here than for $n = 1$. Although for $1/\phi^2$ potential, the data does not allow for a non-accelerating universe, a larger allowed range for w_0 is obtained. (iv) For HIIG observations, $n = 2$ provides a larger range of allowed values of the parameters than $n = 1$. (v) For SN+Hz data, the H_0 and Ω_m constraints are as narrow as in $n = 1$ case, but the observations prefer negative value for C .

From Figure 20, we see that the four data sets do not provide a lower limit on w_0 . Hz data provides an upper limit of -0.68 within 1σ and $w_0 = 0.03$ within 3σ region, showing that this particular model does not allow for a non-accelerating universe within 1σ region. The allowed ranges are almost the same as in the case $n = 1$.

BAO+Hz observation does not allow for a non-accelerating Universe within the 3σ region, and the allowed range for w_0 is wider as compared to the $n = 1$ case. The HIIG data also allows a slightly wider range for w_0 , with the 3σ upper limit being -0.749 and allows the entire range of Ω_m considered in the analysis. The SN+Hz data also allows a wider range for w_0 and Ω_m as compared to $n = 1$ case. Apart from Hz data, the three remaining observational data sets considered in the analysis do not allow for a non-accelerating universe for both $n = 1$ and 2 . For w_0 , Hz observations provide the widest allowed range within 3σ confidence level.

D Evolution of scalar perturbations for ϕ^{-2} potential

For completeness, in this Appendix, we present the evolution of the matter density perturbation δ_m and related quantities for $n = 2$ in the quintessence potential (3.1). Note that in Sec. 4, we presented the detailed analysis for $n = 1$. As mentioned earlier, the evolution of the perturbed quantities is not sensitive to n .

D.1 Evolution of the scaled interaction function δq

Figure 21 is the plot of δq (cf. Eq. 4.8) as a function of N for different k values. Comparing this plot with the plots in Figure 4, we see that evolution of the interaction function is roughly the same for the both the cases. Hence, the evolution of scaled interaction function δq is not sensitive to n .

D.2 Structure formation

Figures 22 and 23 contain plots of δ_m as a function of N for different length scales in interacting and non-interacting scenarios. Figures 24 and 25 contain the plots of $\Delta\delta_m$ and $\Delta\delta_{m_{rel}}$ as a function of N for different length scales, respectively. Thus, we see that evolution of δ_m is roughly the same for $n = 1$ and $n = 2$.

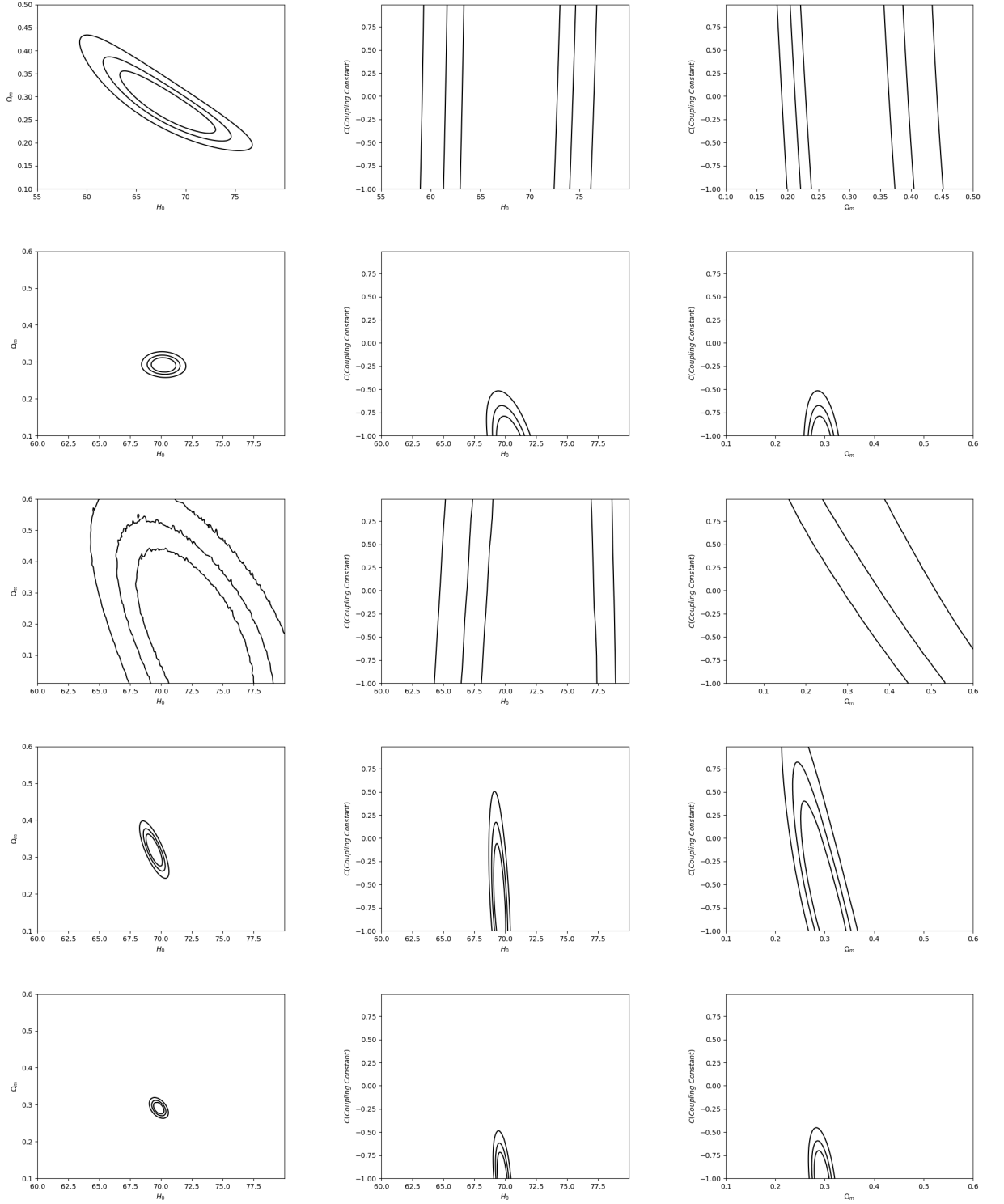


Figure 19. 1,2,3- σ likelihood contours for Hz data (I row), BAO+Hz data (II row), HIIG data (III row), SN+Hz data (IV row) and all four data sets (V row). The two-dimensional contours are obtained by performing marginalization over other parameters.

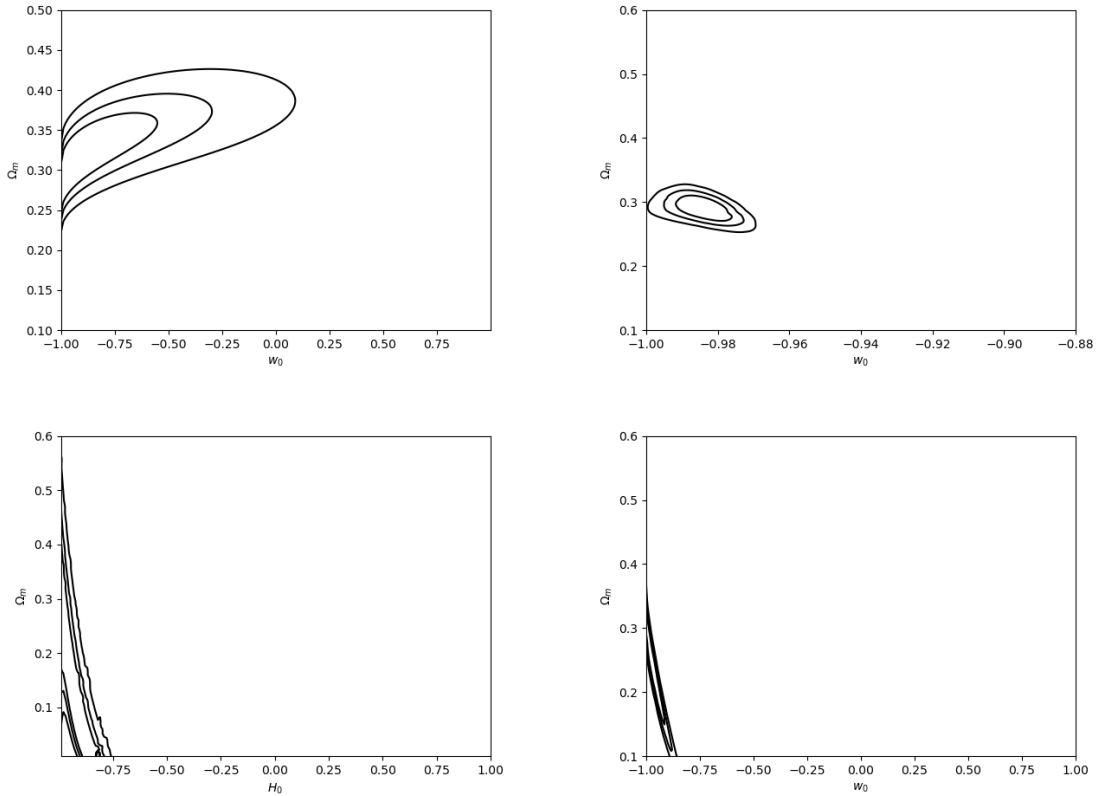


Figure 20. 1,2,3- σ likelihood contours in ‘ w_0 - Ω_m ’ plane. The top row shows constraints from Hz data (left) and BAO+Hz observations (right). The second row shows constraints from HIIG measurements (left) and SN+Hz observations (right).

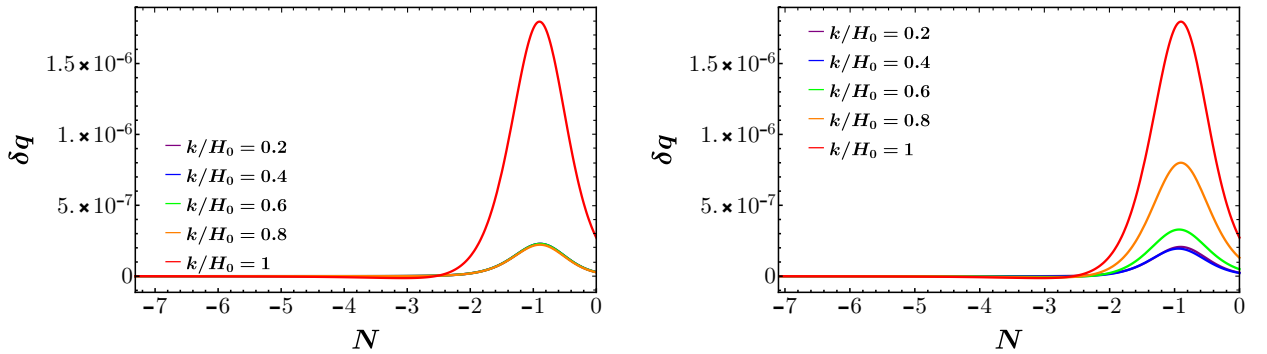


Figure 21. Evolution of δq as a function of N for different values of k with $C = -0.6$

D.3 Weak gravitational lensing

Figures 26 and 27 contain plots of Φ as a function of N for different length scales in interacting and non-interacting Figures 28 and 29 contain the plots of $\Delta\Phi$ and $\Delta\Phi/\Phi_{ni}$ as a function of N for different length scales, respectively. Thus, we see that evolution of Φ is roughly the same for the both the cases and is not sensitive to n .

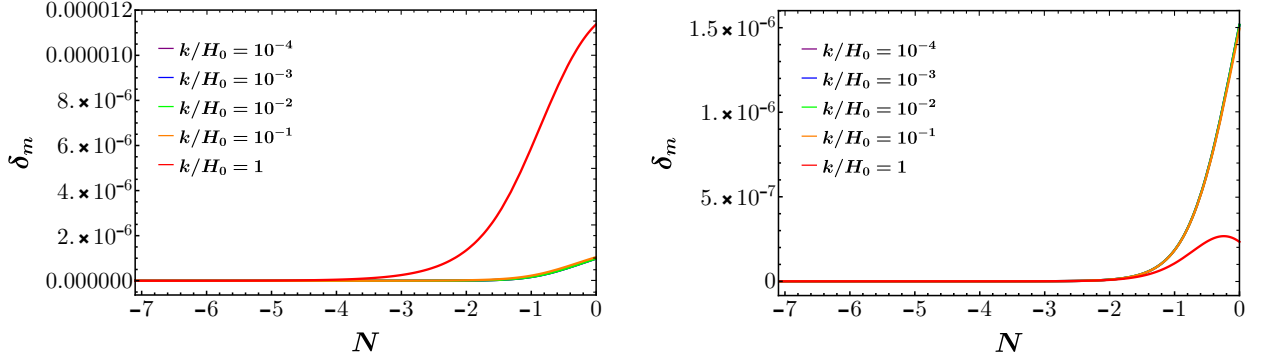


Figure 22. Evolution of δ_m as a function of N . Left: $C = -0.6$, Right: $C = 0$.

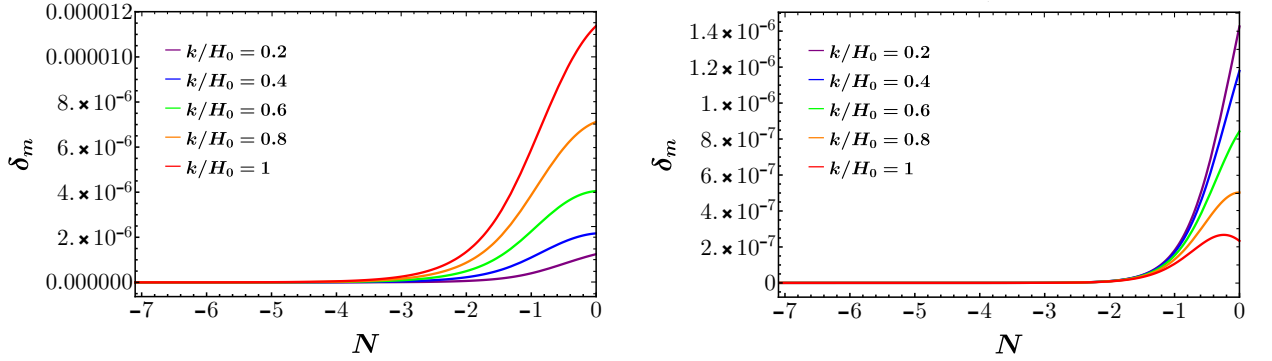


Figure 23. Evolution of δ_m as a function of N . Left: $C = -0.6$, Right: $C = 0$.

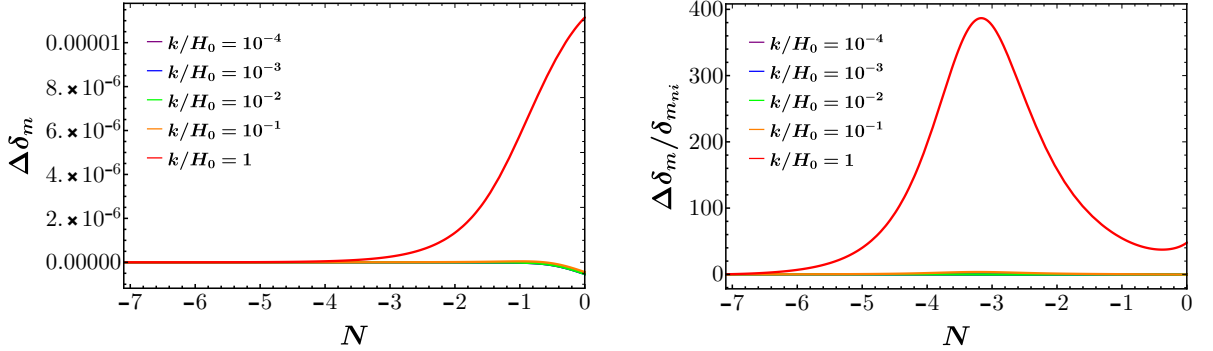


Figure 24. Evolution of $\Delta\delta_m$ (left), $\Delta\delta_m/\delta_{m_{ni}}$ (right) as a function of N .

D.4 ISW effect

Figures 30 and 31 contain plots of Φ' as a function of N for different length scales in interacting and non-interacting Figures 32 and 33 contain the plots of $\Delta\Phi'$ and $\Delta\Phi'/\Phi'_{ni}$ as a function of N for different length scales, respectively. Thus, we see that evolution of Φ' is roughly the same for the both the cases and is not sensitive to n .

We thus conclude that the evolution of δ_m , Φ , and Φ' for the inverse square potential

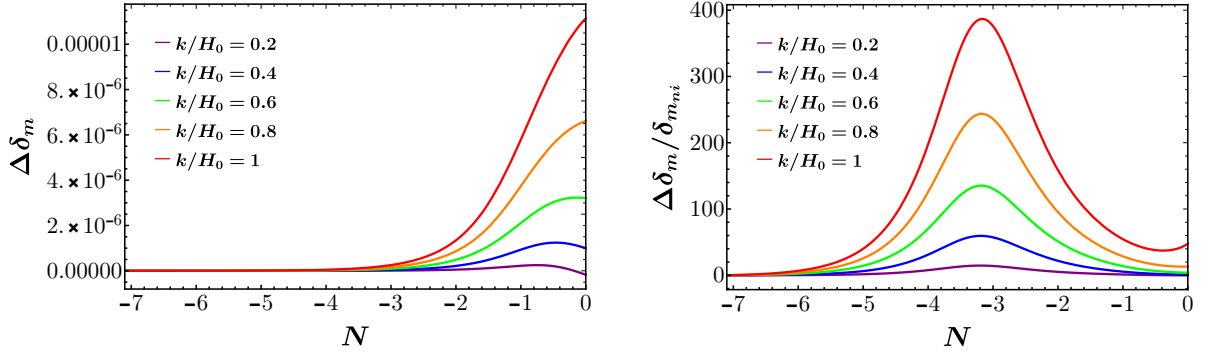


Figure 25. Evolution of $\Delta\delta_m$ (left), $\Delta\delta_m/\delta_{m_{ni}}$ (right) as a function of N .

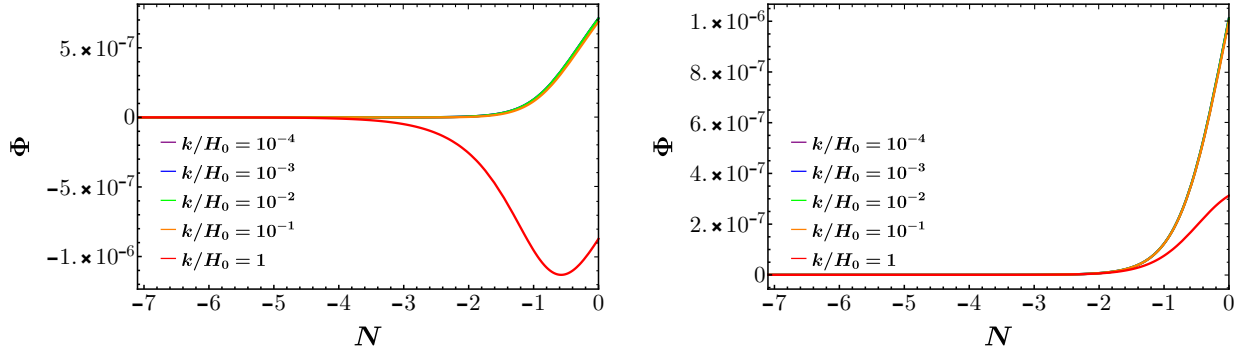


Figure 26. Evolution of Φ as a function of N . Left: $C = -0.6$, Right: $C = 0$.

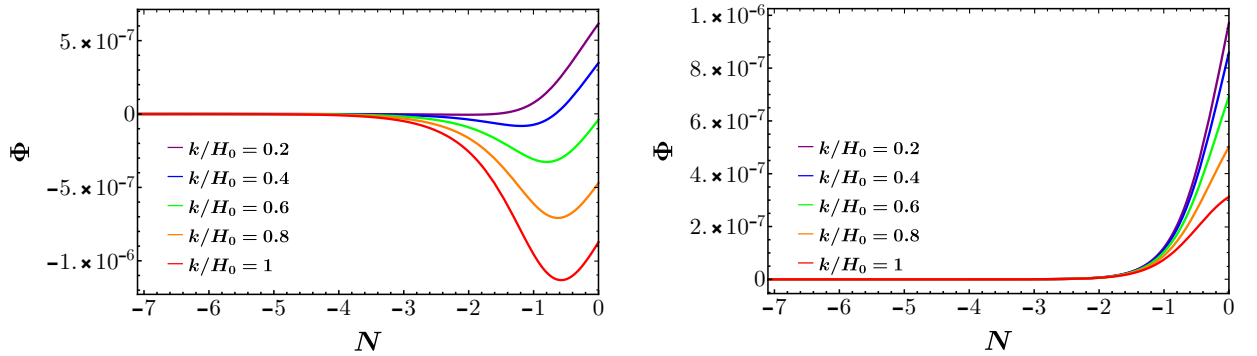


Figure 27. Evolution of Φ as a function of N . Left: $C = -0.6$, Right: $C = 0$.

follow a similar trend as compared to the $U(\phi) \sim 1/\phi$ case. The difference in the evolution becomes significant for $z < 20$, for all length scales. This means that cosmological observations related to the formation of large-scale structures can potentially detect the signatures of dark matter - dark energy interaction.

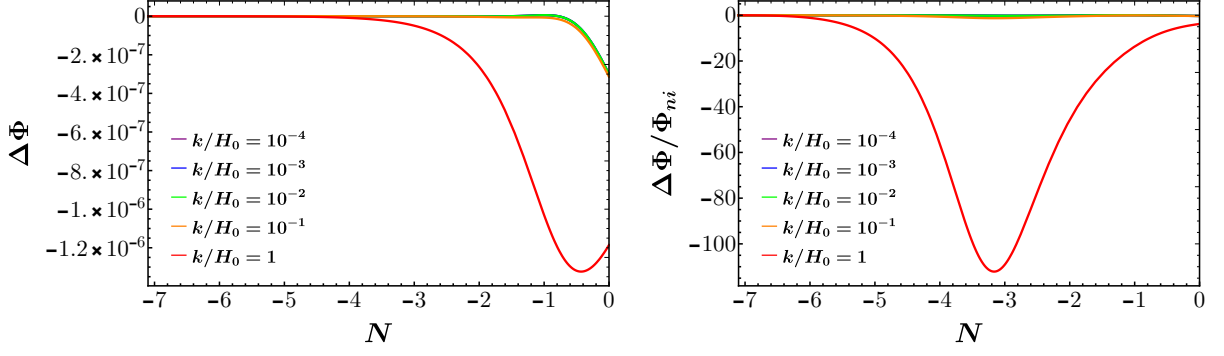


Figure 28. Evolution of $\Delta\Phi$ (left), $\Delta\Phi/\Phi_{ni}$ (right) as a function of N .

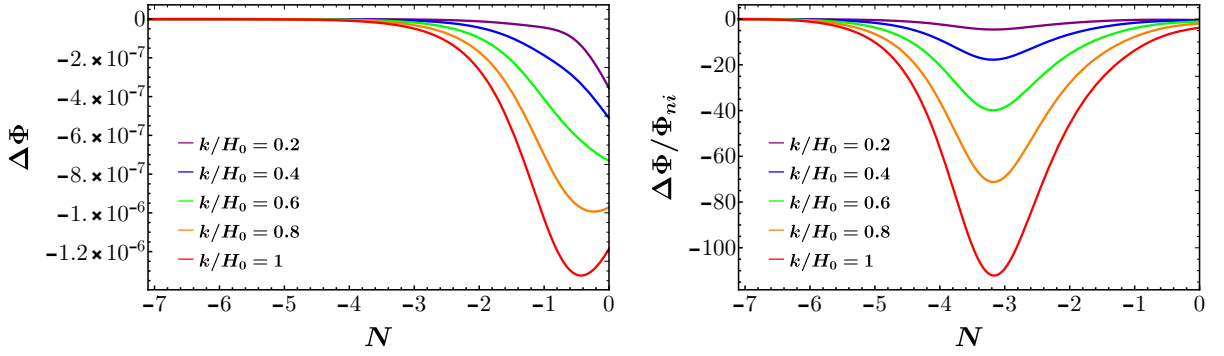


Figure 29. Evolution of $\Delta\Phi$ (left), $\Delta\Phi/\Phi_{ni}$ (right) as a function of N .

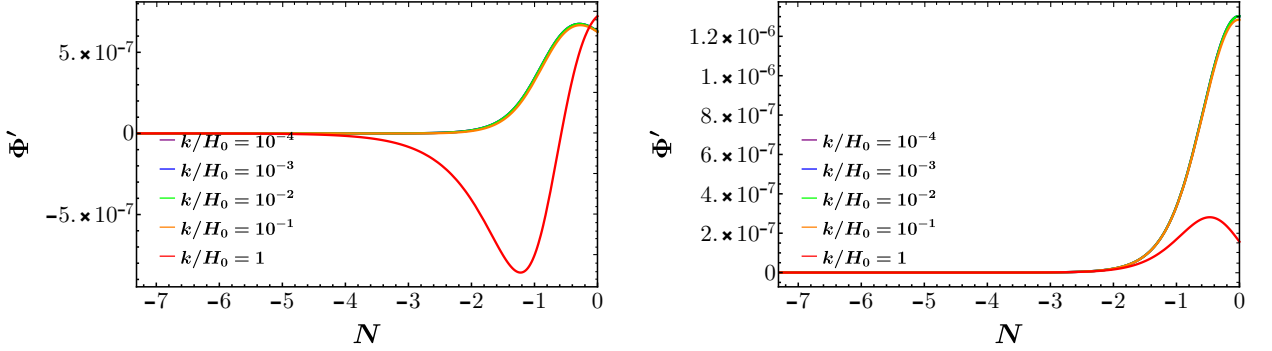


Figure 30. Evolution of Φ' as a function of N . Left: $C = -0.6$, Right: $C = 0$.

E Sound speed of the scalar field

Sound speed and adiabatic sound speed of the dark energy scalar field (ϕ) is given by [120]

$$c_s^2 = \frac{\delta p_\phi}{\delta \rho_\phi}, \quad c_{s_{ad}}^2 = \frac{\dot{p}_\phi}{\dot{\rho}_\phi} = -1 - \frac{2\ddot{\phi}}{3H\dot{\phi} + 2\alpha_\phi \bar{\rho}_m M_{Pl}^2} \quad (\text{E.1})$$

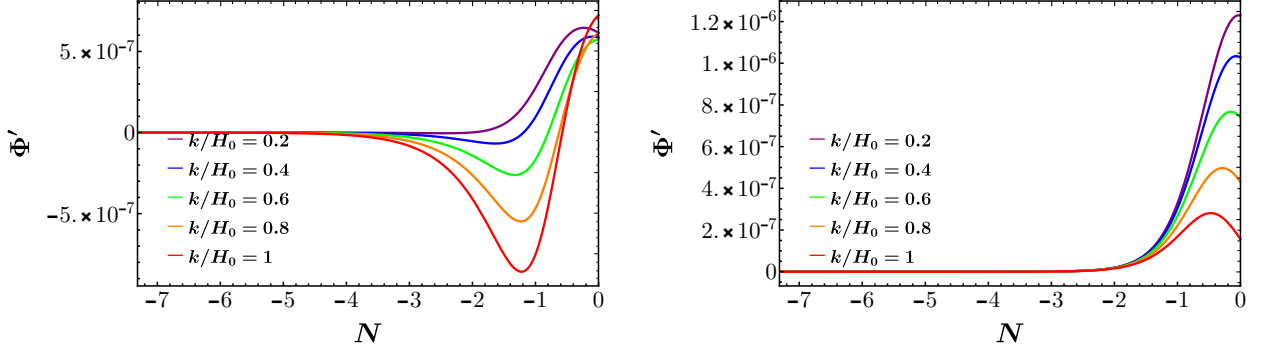


Figure 31. Evolution of Φ' as a function of N . Left: $C = -0.6$, Right: $C = 0$.

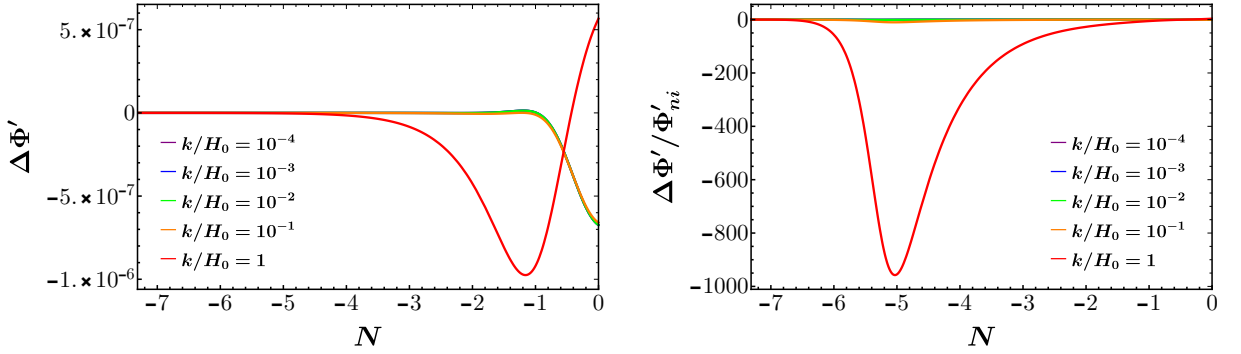


Figure 32. Evolution of $\Delta\Phi'$ (left), $\Delta\Phi'/\Phi'_{ni}$ (right) as a function of N .

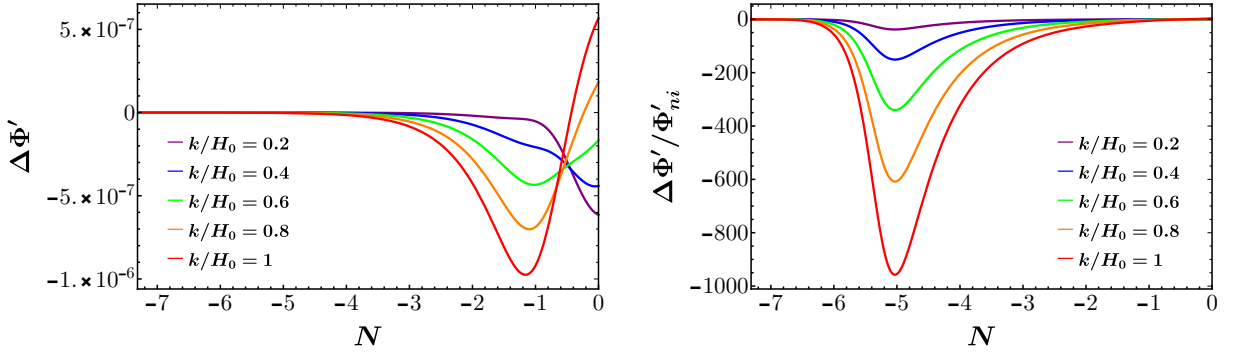


Figure 33. Evolution of $\Delta\Phi'$ (left), $\Delta\Phi'/\Phi'_{ni}$ (right) as a function of N .

In terms of the dimensionless variables, these quantities can be expressed as

$$c_{sad}^2 = \frac{h'(x^2 - y^2) + h(xx' - yy')}{h'(x^2 + y^2) + h(xx' + yy')} = -1 - \frac{2\left(x' + \frac{h'}{h}\right)}{\sqrt{3}(\sqrt{12}x - \sqrt{2}\alpha\beta\Omega_m)} \quad (\text{E.2})$$

$$c_s^2 = \frac{12\Phi x^2 - 2\sqrt{3}x\delta\phi' - 3\sqrt{2}\lambda y^2\delta\phi}{12\Phi x^2 - 2\sqrt{3}x\delta\phi' + 3\sqrt{2}\lambda y^2\delta\phi} \quad (\text{E.3})$$

For a quintessence model, $c_s^2 = 1$ in the rest frame of ϕ [121]. In this work, the perturbed quantities are evaluated in the dark matter rest frame.

References

- [1] A. G. Riess and Others, Observational evidence from supernovae for an accelerating universe and a cosmological constant, [*Astron. J.* **116** \(1998\) 1009](#) [[astro-ph/9805201](#)].
- [2] S. Perlmutter and Others, Measurements of Omega and Lambda from 42 high redshift supernovae, [*Astrophys. J.* **517** \(1999\) 565](#) [[astro-ph/9812133](#)].
- [3] D. N. Spergel and Others, Wilkinson Microwave Anisotropy Probe (WMAP) three year results: implications for cosmology, [*Astrophys. J. Suppl.* **170** \(2007\) 377](#) [[astro-ph/0603449](#)].
- [4] D. M. Scolnic and Others, The Complete Light-curve Sample of Spectroscopically Confirmed SNe Ia from Pan-STARRS1 and Cosmological Implications, [*Astrophys. J.* **859** \(2018\) 101](#) [[1710.00845](#)].
- [5] PLANCK collaboration, Planck 2018 results. I. Overview and the cosmological legacy of Planck, [*Astron. Astrophys.* **641** \(2018\) A1](#) [[1807.06205](#)].
- [6] PLANCK collaboration, Planck 2018 results. vi. cosmological parameters, [*Astron. Astrophys.* **641** \(2020\) A6](#) [[1807.06209](#)].
- [7] T. Padmanabhan, Theoretical Astrophysics: Volume 3, Galaxies and Cosmology, Theoretical Astrophysics. Cambridge University Press, 2000.
- [8] V. Mukhanov, Physical Foundations of Cosmology. Cambridge University Press, 2005, [10.1017/CBO9780511790553](#).
- [9] S. Weinberg, Cosmology, Cosmology. OUP Oxford, 2008.
- [10] D. S. Gorbunov and V. A. Rubakov, Introduction to the Theory of the Early Universe. World Scientific Publishing Company, 2011, [10.1142/7874](#).
- [11] V. Marra, L. Amendola, I. Sawicki and W. Valkenburg, Cosmic variance and the measurement of the local hubble parameter, [*Phys. Rev. Lett.* **110** \(2013\) 241305](#) [[1303.3121](#)].
- [12] L. Verde, P. Protopapas and R. Jimenez, Planck and the local universe: Quantifying the tension, [*Phys. Dark Univ.* **2** \(2013\) 166](#) [[1306.6766](#)].
- [13] C. L. Bennett, D. Larson, J. L. Weiland and G. Hinshaw, The 1% concordance hubble constant, [*Astrophys. J.* **794** \(2014\) 135](#) [[1406.1718](#)].
- [14] A. G. Riess et al., A 2.4% determination of the local value of the hubble constant, [*Astrophys. J.* **826** \(2016\) 56](#) [[1604.01424](#)].
- [15] A. G. Riess, S. Casertano, W. Yuan, L. M. Macri and D. Scolnic, Large magellanic cloud cepheid standards provide a 1% foundation for the determination of the hubble constant and stronger evidence for physics beyond Λ cdm, [*Astrophys. J.* **876** \(2019\) 85](#) [[1903.07603](#)].
- [16] B. Ratra and P. J. E. Peebles, Cosmological consequences of a rolling homogeneous scalar field, [*Phys. Rev. D* **37** \(1988\) 3406](#).
- [17] E. J. Copeland, M. Sami and S. Tsujikawa, Dynamics of dark energy, [*Int. J. Mod. Phys. D* **15** \(2006\) 1753](#) [[hep-th/0603057](#)].
- [18] L. Amendola, Perturbations in a coupled scalar field cosmology, [*Mon. Not. Roy. Astron. Soc.* **312** \(2000\) 521](#) [[astro-ph/9906073](#)].

- [19] L. Amendola, Coupled quintessence, [Phys. Rev. D **62** \(2000\) 043511](#) [[astro-ph/9908023](#)].
- [20] A. P. Billyard and A. A. Coley, Interactions in scalar field cosmology, [Phys. Rev. D **61** \(2000\) 083503](#) [[astro-ph/9908224](#)].
- [21] G. Olivares, F. Atrio-Barandela and D. Pavon, Observational constraints on interacting quintessence models, [Phys. Rev. D **71** \(2005\) 063523](#) [[astro-ph/0503242](#)].
- [22] L. Amendola, G. Camargo Campos and R. Rosenfeld, Consequences of dark matter-dark energy interaction on cosmological parameters derived from SNIa data, [Phys. Rev. D **75** \(2007\) 083506](#) [[astro-ph/0610806](#)].
- [23] G. Olivares, F. Atrio-Barandela and D. Pavon, Dynamics of Interacting Quintessence Models: Observational Constraints, [Phys. Rev. D **77** \(2008\) 063513](#) [[0706.3860](#)].
- [24] C. G. Boehmer, G. Caldera-Cabral, R. Lazkoz and R. Maartens, Dynamics of dark energy with a coupling to dark matter, [Phys. Rev. D **78** \(2008\) 023505](#) [[0801.1565](#)].
- [25] G. Caldera-Cabral, R. Maartens and L. Urena-Lopez, Dynamics of interacting dark energy, [Phys. Rev. D **79** \(2009\) 063518](#) [[0812.1827](#)].
- [26] J.-H. He and B. Wang, Effects of the interaction between dark energy and dark matter on cosmological parameters, [JCAP **06** \(2008\) 010](#) [[0801.4233](#)].
- [27] V. Pettorino and C. Baccigalupi, Coupled and Extended Quintessence: theoretical differences and structure formation, [Phys. Rev. D **77** \(2008\) 103003](#) [[0802.1086](#)].
- [28] M. Quartin, M. O. Calvao, S. E. Joras, R. R. Reis and I. Waga, Dark Interactions and Cosmological Fine-Tuning, [JCAP **05** \(2008\) 007](#) [[0802.0546](#)].
- [29] C. G. Boehmer, G. Caldera-Cabral, N. Chan, R. Lazkoz and R. Maartens, Quintessence with quadratic coupling to dark matter, [Phys. Rev. D **81** \(2010\) 083003](#) [[0911.3089](#)].
- [30] J. Beyer, S. Nurmi and C. Wetterich, Coupled dark energy and dark matter from dilatation anomaly, [Phys. Rev. D **84** \(2011\) 023010](#) [[1012.1175](#)].
- [31] L. Lopez Honorez, O. Mena and G. Panotopoulos, Higher-order coupled quintessence, [Phys. Rev. D **82** \(2010\) 123525](#) [[1009.5263](#)].
- [32] P. Avelino and H. da Silva, Effective dark energy equation of state in interacting dark energy models, [Phys. Lett. B **714** \(2012\) 6](#) [[1201.0550](#)].
- [33] S. Pan, S. Bhattacharya and S. Chakraborty, An analytic model for interacting dark energy and its observational constraints, [Mon. Not. Roy. Astron. Soc. **452** \(2015\) 3038](#) [[1210.0396](#)].
- [34] V. Salvatelli, A. Marchini, L. Lopez-Honorez and O. Mena, New constraints on Coupled Dark Energy from the Planck satellite experiment, [Phys. Rev. D **88** \(2013\) 023531](#) [[1304.7119](#)].
- [35] L. P. Chimento, M. G. Richarte and I. E. Sánchez García, Interacting dark sector with variable vacuum energy, [Phys. Rev. D **88** \(2013\) 087301](#) [[1310.5335](#)].

- [36] L. Amendola, T. Barreiro and N. J. Nunes, Multifield coupled quintessence, [Phys. Rev. D](#) **90** (2014) 083508 [[1407.2156](#)].
- [37] B. Wang, E. Abdalla, F. Atrio-Barandela and D. Pavon, Dark Matter and Dark Energy Interactions: Theoretical Challenges, Cosmological Implications and Observations, [Rept. Prog. Phys.](#) **79** (2016) 096901 [[1603.08299](#)].
- [38] V. Marra, Coupling dark energy to dark matter inhomogeneities, [Phys. Dark Univ.](#) **13** (2016) 25 [[1506.05523](#)].
- [39] F. F. Bernardi and R. G. Landim, Coupled quintessence and the impossibility of an interaction: a dynamical analysis study, [Eur. Phys. J. C](#) **77** (2017) 290 [[1607.03506](#)].
- [40] S. Pan and G. Sharov, A model with interaction of dark components and recent observational data, [Mon. Not. Roy. Astron. Soc.](#) **472** (2017) 4736 [[1609.02287](#)].
- [41] C. Van De Bruck and J. Mifsud, Searching for dark matter - dark energy interactions: going beyond the conformal case, [Phys. Rev. D](#) **97** (2018) 023506 [[1709.04882](#)].
- [42] M. Carrillo González and M. Trodden, Field Theories and Fluids for an Interacting Dark Sector, [Phys. Rev. D](#) **97** (2018) 043508 [[1705.04737](#)].
- [43] B. J. Barros, L. Amendola, T. Barreiro and N. J. Nunes, Coupled quintessence with a Λ CDM background: removing the σ_8 tension, [JCAP](#) **01** (2019) 007 [[1802.09216](#)].
- [44] R. G. Landim, Cosmological perturbations and dynamical analysis for interacting quintessence, [Eur. Phys. J. C](#) **79** (2019) 889 [[1908.03657](#)].
- [45] E. Di Valentino, A. Melchiorri and O. Mena, Can interacting dark energy solve the H_0 tension?, [Phys. Rev. D](#) **96** (2017) 043503 [[1704.08342](#)].
- [46] S. Kumar and R. C. Nunes, Echo of interactions in the dark sector, [Phys. Rev. D](#) **96** (2017) 103511 [[1702.02143](#)].
- [47] W. Yang, A. Mukherjee, E. Di Valentino and S. Pan, Interacting dark energy with time varying equation of state and the H_0 tension, [Phys. Rev. D](#) **98** (2018) 123527 [[1809.06883](#)].
- [48] W. Yang, S. Pan, E. Di Valentino, R. C. Nunes, S. Vagnozzi and D. F. Mota, Tale of stable interacting dark energy, observational signatures, and the H_0 tension, [JCAP](#) **09** (2018) 019 [[1805.08252](#)].
- [49] S. Pan, W. Yang, E. Di Valentino, E. N. Saridakis and S. Chakraborty, Interacting scenarios with dynamical dark energy: Observational constraints and alleviation of the H_0 tension, [Phys. Rev. D](#) **100** (2019) 103520 [[1907.07540](#)].
- [50] E. Di Valentino, A. Melchiorri, O. Mena and S. Vagnozzi, Nonminimal dark sector physics and cosmological tensions, [Phys. Rev. D](#) **101** (2020) 063502 [[1910.09853](#)].
- [51] A. Gómez-Valent, V. Pettorino and L. Amendola, Update on coupled dark energy and the h_0 tension, [Phys. Rev. D](#) **101** (2020) 123513 [[2004.00610](#)].
- [52] J. P. Johnson and S. Shankaranarayanan, Cosmological perturbations in the interacting dark sector: Mapping fields and fluids, [Phys. Rev. D](#) **103** (2021) 023510 [[2006.04618](#)].

- [53] A. Pavlov, S. Westmoreland, K. Saaidi and B. Ratra, Nonflat time-variable dark energy cosmology, [*Phys. Rev. D* **88** \(2013\) 123513](#) [[1307.7399](#)].
- [54] O. Farooq, F. R. Madiyar, S. Crandall and B. Ratra, Hubble parameter measurement constraints on the redshift of the deceleration–acceleration transition, dynamical dark energy, and space curvature, [*Astrophys. J.* **835** \(2017\) 26](#) [[1607.03537](#)].
- [55] J. Simon, L. Verde and R. Jimenez, Constraints on the redshift dependence of the dark energy potential, [*Phys. Rev. D* **71** \(2005\) 123001](#) [[astro-ph/0412269](#)].
- [56] D. Stern, R. Jimenez, L. Verde, S. A. Stanford and M. Kamionkowski, Cosmic Chronometers: Constraining the Equation of State of Dark Energy. II. A Spectroscopic Catalog of Red [*Astrophys. J. Suppl.* **188** \(2010\) 280](#) [[0907.3152](#)].
- [57] M. Moresco et al., Improved constraints on the expansion rate of the universe up to $z \sim 1.1$ from the spectroscopic evolution of cosmic chronometers, [*JCAP* **08** \(2012\) 006](#) [[1201.3609](#)].
- [58] M. Moresco, L. Pozzetti, A. Cimatti, R. Jimenez, C. Maraston, L. Verde et al., A 6% measurement of the hubble parameter at $z \sim 0.45$: direct evidence of the epoch of cosmic re-acceleration, [*JCAP* **05** \(2016\) 014](#) [[1601.01701](#)].
- [59] M. Moresco, Raising the bar: new constraints on the hubble parameter with cosmic chronometers at $z \sim 2$, [*Mon. Not. Roy. Astron. Soc.* **450** \(2015\) L16](#) [[1503.01116](#)].
- [60] C. Zhang, H. Zhang, S. Yuan, T.-J. Zhang and Y.-C. Sun, Four new observational $h(z)$ data from luminous red galaxies in the sloan digital sky survey data release seven, [*Res. Astron. Astrophys.* **14** \(2014\) 1221](#) [[1207.4541](#)].
- [61] A. L. Ratsimbazafy, S. I. Loubser, S. M. Crawford, C. M. Cress, B. A. Bassett, R. C. Nichol et al., Age-dating luminous red galaxies observed with the southern african large telescope, [*Mon. Not. Roy. Astron. Soc.* **467** \(2017\) 3239](#) [[1702.00418](#)].
- [62] A. L. González-Morán, R. Chávez, R. Terlevich, E. Terlevich, F. Bresolin, D. Fernández-Arenas et al., Independent cosmological constraints from high- z H ii galaxies, [*Mon. Not. Roy. Astron. Soc.* **487** \(2019\) 4669](#) [[1906.02195](#)].
- [63] R. Chávez, R. Terlevich, E. Terlevich, F. Bresolin, J. Melnick, M. Plionis et al., The $1 - \sigma$ relation for massive bursts of star formation, [*Mon. Not. Roy. Astron. Soc.* **442** \(2014\) 3565](#) [[1405.4010](#)].
- [64] D. K. Erb, C. C. Steidel, A. E. Shapley, M. Pettini, N. A. Reddy and K. L. Adelberger, The stellar, gas and dynamical masses of star-forming galaxies at $z \sim 2$, [*Astrophys. J.* **646** \(2006\) 107](#) [[astro-ph/0604041](#)].
- [65] D. Masters et al., Physical properties of emission-line galaxies at $z \sim 2$ from near-infrared spectroscopy with magellan fire, [*Astrophys. J.* **785** \(2014\) 153](#) [[1402.0510](#)].
- [66] M. V. Maseda et al., The nature of extreme emission line galaxies at $z=1-2$: Kinematics and metallicities from near-infrared spectroscopy, [*Astrophys. J.* **791** \(2014\) 17](#) [[1406.3351](#)].
- [67] R. Terlevich, E. Terlevich, J. Melnick, R. Chávez, M. Plionis, F. Bresolin et al., On the road to precision cosmology with high-redshift h ii galaxies, [*Mon. Not. Roy. Astron. Soc.* **451** \(2015\) 3001](#) [[1505.04376](#)].
- [68] BOSS collaboration, The clustering of galaxies in the completed sdss-iii baryon oscillation spectroscopic survey: cosmological analysis of the dr12 galaxy sample, [*Mon. Not. Roy. Astron. Soc.* **470** \(2017\) 2617](#) [[1607.03155](#)].
- [69] F. Beutler, C. Blake, M. Colless, D. H. Jones, L. Staveley-Smith, L. Campbell et al., The 6df galaxy survey: Baryon acoustic oscillations and the local hubble constant, [*Mon. Not. Roy. Astron. Soc.* **416** \(2011\) 3017](#) [[1106.3366](#)].

- [70] A. J. Ross, L. Samushia, C. Howlett, W. J. Percival, A. Burden and M. Manera, The clustering of the sdss dr7 main galaxy sample – i. a 4 per cent distance measure at $z = 0.15$, [Mon. Not. Roy. Astron. Soc. **449** \(2015\) 835 \[1409.3242\]](#).
- [71] M. Ata et al., The clustering of the sdss-iv extended baryon oscillation spectroscopic survey dr14 quasar sample: first measurement of baryon acoustic oscillations between redshift 0.8 and 2.2, [Mon. Not. Roy. Astron. Soc. **473** \(2018\) 4773 \[1705.06373\]](#).
- [72] J. E. Bautista et al., Measurement of baryon acoustic oscillation correlations at $z = 2.3$ with sdss dr12 $\text{Ly}\alpha$ -forests, [Astron. Astrophys. **603** \(2017\) A12 \[1702.00176\]](#).
- [73] SDSS collaboration, Improved cosmological constraints from a joint analysis of the sdss-ii and snls supernova samples, [Astron. Astrophys. **568** \(2014\) A22 \[1401.4064\]](#).
- [74] A. G. Riess et al., New parallaxes of galactic cepheids from spatially scanning the hubble space telescope: Implications for the hubble constant, [Astrophys. J. **855** \(2018\) 136 \[1801.01120\]](#).
- [75] J. Ryan, S. Doshi and B. Ratra, Constraints on dark energy dynamics and spatial curvature from hubble parameter and baryon acoustic oscillation data, [Mon. Not. Roy. Astron. Soc. **480** \(2018\) 759 \[1805.06408\]](#).
- [76] J. Ooba, B. Ratra and N. Sugiyama, Planck 2015 constraints on the nonflat ϕ cdm inflation model, [Astrophys. J. **866** \(2018\) 68 \[1712.08617\]](#).
- [77] X.-W. Liu, C. Heneka and L. Amendola, Constraining coupled quintessence with the 21cm signal, [JCAP **05** \(2020\) 038 \[1910.02763\]](#).
- [78] M.-J. Zhang and H. Li, Observational constraint on the dark energy scalar field, [1809.08936](#).
- [79] A. Sangwan, A. Tripathi and H. K. Jassal, Observational constraints on quintessence models of dark energy, [1804.09350](#).
- [80] N. Khadka and B. Ratra, Using quasar x-ray and uv flux measurements to constrain cosmological model parameters, [Mon. Not. Roy. Astron. Soc. **497** \(2020\) 263 \[2004.09979\]](#).
- [81] L. A. Ureña López and N. Roy, Generalized tracker quintessence models for dark energy, [Phys. Rev. D **102** \(2020\) 063510 \[2007.08873\]](#).
- [82] N. Khadka and B. Ratra, Constraints on cosmological parameters from gamma-ray burst peak photon energy and bolometric fluence measurements and other data, [Mon. Not. Roy. Astron. Soc. **499** \(2020\) 391 \[2007.13907\]](#).
- [83] S. Cao, J. Ryan and B. Ratra, Using pantheon and des supernova, baryon acoustic oscillation, and hubble parameter data to constrain the hubble constant, dark energy dynamics, and spatial curvature, [2101.08817](#).
- [84] D. Stern, R. Jimenez, L. Verde, M. Kamionkowski and S. A. Stanford, Cosmic chronometers: constraining the equation of state of dark energy. I: $H(z)$ measurements, [JCAP **2010** \(2010\) 008 \[0907.3149\]](#).
- [85] E. Gaztañaga, A. Cabré and L. Hui, Clustering of luminous red galaxies - iv. baryon acoustic peak in the line-of-sight direction and a direct measurement of $h(z)$, [Mon. Not. Roy. Astron. Soc. **399** \(2009\) 1663 \[0807.3551\]](#).
- [86] SDSS collaboration, The data release of the sloan digital sky survey-ii supernova survey, [Publ. Astron. Soc. Pac. **130** \(2018\) 064002 \[1401.3317\]](#).
- [87] SNLS collaboration, Supernova constraints and systematic uncertainties from the first 3 years of the supernova legacy survey, [Astrophys. J. Suppl. **192** \(2011\) 1 \[1104.1443\]](#).
- [88] C. Balland et al., The eso's vlt type ia supernova spectral set of the final two years of snls, [Astron. Astrophys. **614** \(2018\) A134 \[1712.07379\]](#).

- [89] SNLS collaboration, The supernova legacy survey 3-year sample: Type ia supernovae photometric distances and cosmological constraints, [*Astron. Astrophys.* **523** \(2010\) A7](#) [[1010.4743](#)].
- [90] C.-H. Chuang and Y. Wang, Modeling the anisotropic two-point galaxy correlation function on small scales and improved measurements of $h(z)$, $d_a(z)$, and $\beta(z)$ from the sloan digital sky survey dr7 luminous red galaxies, [*Mon. Not. Roy. Astron. Soc.* **435** \(2013\) 255](#) [[1209.0210](#)].
- [91] N. G. Busca et al., Baryon acoustic oscillations in the ly- α forest of boss quasars, [*Astron. Astrophys.* **552** \(2013\) A96](#) [[1211.2616](#)].
- [92] C. Blake et al., The wigglez dark energy survey: Joint measurements of the expansion and growth history at $z < 1$, [*Mon. Not. Roy. Astron. Soc.* **425** \(2012\) 405](#) [[1204.3674](#)].
- [93] E. Aubourg et al., Cosmological implications of baryon acoustic oscillation measurements, [*Phys. Rev. D* **92** \(2015\) 123516](#) [[1411.1074](#)].
- [94] SDSS collaboration, Detection of the baryon acoustic peak in the large-scale correlation function of sdss luminous red galaxies, [*Astrophys. J.* **633** \(2005\) 560](#) [[astro-ph/0501171](#)].
- [95] K. D. Gordon, G. C. Clayton, K. A. Misselt, A. U. Landolt and M. J. Wolff, A quantitative comparison of the small magellanic cloud, large magellanic cloud, and milky way ultraviolet to near-infrared extinction curves, [*The Astrophysical Journal* **594** \(2003\) 279](#) [[astro-ph/0305257](#)].
- [96] R. Chavez, E. Terlevich, R. Terlevich, M. Plionis, F. Bresolin, S. Basilakos et al., Determining the hubble constant using giant extragalactic hii regions and hii galaxies, [*Mon. Not. Roy. Astron. Soc.* **425** \(2012\) 56](#) [[1203.6222](#)].
- [97] D. Fernández Arenas, E. Terlevich, R. Terlevich, J. Melnick, R. Chávez, F. Bresolin et al., An independent determination of the local hubble constant, [*Mon. Not. Roy. Astron. Soc.* **474** \(2018\) 1250](#) [[1710.05951](#)].
- [98] S. Cao, J. Ryan and B. Ratra, Cosmological constraints from h ii starburst galaxy apparent magnitude and other cosmological measurements, [*Mon. Not. Roy. Astron. Soc.* **497** \(2020\) 3191](#) [[2005.12617](#)].
- [99] R. Chávez, M. Plionis, S. Basilakos, R. Terlevich, E. Terlevich, J. Melnick et al., Constraining the dark energy equation of state with h II galaxies, [*Mon. Not. Roy. Astron. Soc.* **462** \(2016\) 2431](#) [[1607.06458](#)].
- [100] N. Metropolis, A. W. Rosenbluth, M. N. Rosenbluth, A. H. Teller and E. Teller, Equation of state calculations by fast computing machines, [*J. Chem. Phys.* **21** \(1953\) 1087](#).
- [101] W. K. Hastings, Monte carlo sampling methods using markov chains and their applications, [*Biometrika* **57** \(1970\) 97](#).
- [102] R. M. Neal, Taking bigger metropolis steps by dragging fast variables, [arXiv Mathematics e-prints \(2005\) math/0502099](#) [[math/0502099](#)].
- [103] B. Audren, J. Lesgourgues, K. Benabed and S. Prunet, Conservative constraints on early cosmology: an illustration of the monte python cosmological parameter inference code, [*JCAP* **02** \(2013\) 001](#) [[1210.7183](#)].
- [104] A. Gelman and D. B. Rubin, Inference from iterative simulation using multiple sequences, [*Statist. Sci.* **7** \(1992\) 457](#).
- [105] S. M. Carroll, M. Hoffman and M. Trodden, Can the dark energy equation-of-state parameter w be less than -1 ?, [*Phys. Rev. D* **68** \(2003\) 023509](#) [[astro-ph/0301273](#)].
- [106] A. Bouali, I. Albarran, M. Bouhmadi-López and T. Ouali, Cosmological constraints of phantom dark energy models, [*Phys. Dark Univ.* **26** \(2019\) 100391](#) [[1905.07304](#)].

- [107] S. Birrer et al., H0licow - ix. cosmographic analysis of the doubly imaged quasar sdss 1206+4332 and a new measurement of the hubble constant, [Mon. Not. Roy. Astron. Soc.](#) **484** (2019) 4726 [[1809.01274](#)].
- [108] L. Amendola and Others, Cosmology and fundamental physics with the Euclid satellite, [Living Rev. Rel.](#) **21** (2018) 2 [[1606.00180](#)].
- [109] Y. Gupta, B. Ajithkumar, H. S. Kale, S. Nayak, S. Sabhapathy, S. Sureshkumar et al., The upgraded GMRT: opening new windows on the radio Universe, [Current Science](#) **113** (2017) 707.
- [110] SKA COSMOLOGY SWG collaboration, Overview of cosmology with the ska, [PoS AASKA14](#) (2015) 016 [[1501.04076](#)].
- [111] M. P. van Haarlem et al., Lofar: The low-frequency array, [Astron. Astrophys.](#) **556** (2013) A2 [[1305.3550](#)].
- [112] H. Hildebrandt et al., Kids-450: Cosmological parameter constraints from tomographic weak gravitational lensing, [Mon. Not. Roy. Astron. Soc.](#) **465** (2017) 1454 [[1606.05338](#)].
- [113] C. Heymans et al., Kids-1000 cosmology: Multi-probe weak gravitational lensing and spectroscopic galaxy clustering constraints, [Astron. Astrophys.](#) **646** (2021) A140 [[2007.15632](#)].
- [114] A. J. Nishizawa, The integrated sachs–wolfe effect and the rees–sciama effect, [PTEP](#) **2014** (2014) 06B110 [[1404.5102](#)].
- [115] R. G. Crittenden and N. Turok, Looking for lambda with the rees-sciama effect, [Phys. Rev. Lett.](#) **76** (1996) 575 [[astro-ph/9510072](#)].
- [116] J. P. Johnson and S. Shankaranarayanan, Low-energy modified gravity signatures on the large-scale structures, [Phys. Rev. D](#) **100** (2019) 083526 [[1904.07608](#)].
- [117] W. M. Farr, M. Fishbach, J. Ye and D. Holz, A future percent-level measurement of the hubble expansion at redshift 0.8 with advanced ligo, [Astrophys. J. Lett.](#) **883** (2019) L42 [[1908.09084](#)].
- [118] H. Akaike, A new look at the statistical model identification, [IEEE Transactions on Automatic Control](#) **19** (1974) 716.
- [119] G. Schwarz, Estimating the dimension of a model, [Annals Statist.](#) **6** (1978) 461.
- [120] R. H. Brandenberger, Quantum field theory methods and inflationary universe models, [Rev. Mod. Phys.](#) **57** (1985) 1.
- [121] J. Valiviita, E. Majerotto and R. Maartens, Instability in interacting dark energy and dark matter fluids, [JCAP](#) **07** (2008) 020 [[0804.0232](#)].